Embedding Active Force Control within the Compliant Hybrid Zero Dynamics to Achieve Stable, Fast Running on MABEL

Koushil Sreenath, Hae-Won Park, J. W. Grizzle

***Abstract*—A mathematical formalism for designing provably stable, running gaits in bipedal robots with compliance is presented and the theoretical work is validated experimentally on MABEL, a planar bipedal testbed that contains springs in its drivetrain. The methods of virtual constraints and hybrid zero dynamics are used to design a time-invariant feedback controller that not only respects the natural compliance of the open-loop system, but also enables active force control within the compliant hybrid zero dynamics. The controller dynamically varies the effective leg stiffness throughout the gait. When implemented on MABEL, a kneed-biped running record of 3.06 m/s (10.9 kph or 6.8 mph) is achieved.**

***Index Terms*—Bipedal robots, Running, Hybrid Systems, Zero Dynamics, Compliance, Force Control.**

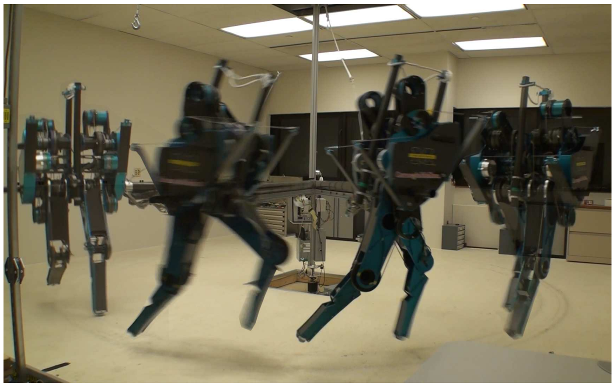

Fig. 1. A composite illustrating the dynamic and agile running gait obtained on MABEL.

I. INTRODUCTION

A model-driven feedback control design is employed to achieve stable, fast running on MABEL, a planar robot with revolute knees and compliance. The resulting nonlinear, compliant hybrid zero dynamics controller with active force control, running in real-time, was instrumental in obtaining fast running at speeds upto 3.06 m/s, with a flight phase of almost 40% of the gait, and with a ground clearance of $7-10$ cm.

A brief background on running robots is provided next, followed by an overview of the experimental testbed and a summary of contributions of the paper.

A. Background

Running is an extremely agile motion, typically characterized by the presence of a flight phase with the feet off the ground. Elegant running gaits were reported by Raibert et al. in 1989 for a monopedal robot with a light, prismatic, spring-loaded leg. Hopping speeds upto 5.9 m/s were achieved with an intuitive controller (Koechling, 1989). Raibert's seminal work inspired a class of models based on a Spring Loaded Inverted Pendulum (SLIP) (Full and Koditschek, 1999), and his collection of control actions for regulating hopping height, torso pitch, and leg angle are commonly referred to as a Raibert controller. Raibert's controllers produce stable running gaits on systems whose dynamics are similar to that of a SLIP, but it is unclear how stable gaits can be achieved on robots with more complicated dynamics, such as revolute knees, legs with significant mass, or a distributed torso (Poulakakis and Grizzle, 2009b).

On bipedal robots that were not specifically conceived for running, the ZMP criterion has been employed to demonstrate running gaits with short flight times and low ground clearance during flight. Examples include Sony's QRIO (Nagasaka et al., 2004), Honda's ASIMO (Hirose and Ogawa, 2007), Toyota's humanoid robot (Tajima et al., 2009) (with running at a top speed of 1.94 m/s), HRP-2LR (Kajita et al., 2005), HRP-2LT (Kajita et al., 2007), and HUBO (Cho et al., 2009). In these robots, some form of ZMP regulation is used during the stance phase to prevent the foot from rolling.

In 2004, running was attempted on RABBIT, a planar robot with revolute knees and no compliance, through a controller based on the hybrid zero dynamics framework (Morris et al., 2006). The obtained running gait had nice qualities, such as a significant flight duration and good ground clearance, however stable running was not obtained. Reasons for this failure included: (a) because the robot had no compliance, its actuators were forced to behave like springs, performing negative work on impact to redirect the COM upwards; (b) the nominal gait required 95% of the motors' maximum torque, leaving

---

Koushil Sreenath and J. W. Grizzle are with the Control Systems Laboratory, Electrical Engineering and Computer Science Department, University of Michigan, Ann Arbor, MI 48109-2122, USA. `{koushils, grizzle}@umich.edu`

Hae-Won. Park is with the Mechanical Engineering Department, University of Michigan, Ann Arbor, MI 48109-2125, USA. `parkhw@umich.edu`

This work is supported in part by NSF grant ECS-909300 and in part by DARPA Contract W91CRB-11-1-0002.

very little torque for feedback correction; and (c) the controller and lack of compliance together resulted in bad ground contact forces during transients (Poulakakis and Grizzle, 2009b). These considerations led to the design of MABEL, a planar biped, which incorporated compliance in the transmission for shock absorption and for energy efficiency. An overview of the experimental testbed is provided next.

B. *Description of MABEL*

MABEL is a planar bipedal robot comprised of five links assembled to form a torso and two legs with knees; see Figure 1. The robot weighs 65 kg, has 1 m long legs, and is mounted on a boom of radius 2.25 m. The legs are terminated in point feet. All actuators are located in the torso, so that the legs are kept as light as possible; this is to facilitate rapid leg swinging for running. Unlike most bipedal robots, the actuated degrees of freedom of each leg do not correspond to the knee and hip angles. Instead, for each leg, a collection of cable-differentials is used to connect two motors to the hip and knee joints in such a way that one motor controls the angle of the virtual leg (henceforth called the leg angle) consisting of the line connecting the hip to the toe, and the second motor is connected in series with a spring in order to control the length or shape of the virtual leg (henceforth called the leg shape); see Figure 2. The motors drive the links through a transmission that comprises of several pulleys connected by cables. The reader is referred to (Park et al., 2011; Grizzle et al., 2009; Hurst, 2008) for more details on the transmission.

The springs in MABEL serve to isolate the reflected rotor inertia of the leg-shape motors from the impact forces at leg touchdown and to store energy in the compression phase of a running gait, when the support leg must decelerate the downward motion of the robot's center of mass; the energy stored in the spring can then be used to redirect the center of mass upwards for the subsequent flight phase, when both legs are off the ground. These properties (shock isolation and energy storage) enhance the energy efficiency of running and reduce the overall actuator power requirements. MABEL has a unilateral spring which compresses but does not extend beyond its rest length. This ensures that springs are present when they are useful for shock attenuation and energy storage, and absent when they would be a hindrance for lifting the legs from the ground.

In (Sreenath et al., 2011), walking controllers were designed for MABEL such that the natural compliant dynamics is preserved in the closed-loop system, ensuring the compliance performs the negative work at impact and thereby resulting in energy efficient walking gaits. Moreover, the nonlinear compliant Hybrid Zero Dynamics controller was implemented on MABEL and was instrumental in obtaining fast walking at a top sustained speed of 1.5 m/s (3.4 mph.)

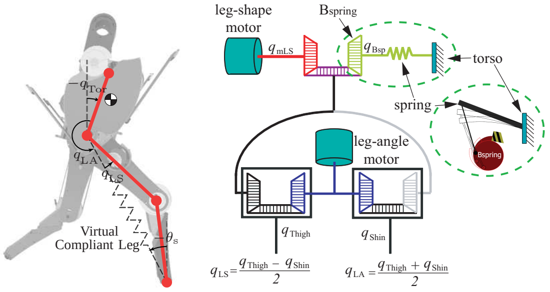

(a) (b)

Fig. 2. (a) The *virtual compliant leg* created by the drivetrain through a set of differentials. The coordinate system used for the linkage is also indicated. Angles are positive in the counter clockwise direction. (b) MABEL's drivetrain (same for each leg), all housed in the torso. Two motors and a spring are connected to the traditional hip and knee joints via three differentials. On the robot, the differentials are realized via cables and pulleys (Hurst, 2008) and not via gears. They are connected such that the actuated variables are leg angle and leg shape, so that the spring is in series with the leg shape motor. The base of the spring is grounded to the torso and the other end is connected to the $\mathrm{B_{spring}}$ differential via a cable, which makes the spring *unilateral*. When the spring reaches its rest length, the pulley hits a hardstop, formed by a very stiff damper. When this happens, the leg shape motor is, for all intents and purposes, rigidly connected to leg shape through a gear ratio.

C. *Contributions*

The key results of the paper are summarized next. A HZD-based controller is designed for running such that the natural compliant dynamics is preserved as the dominant characteristic of the closed-loop system resulting in a compliant hybrid zero dynamics. Furthermore, the choice of the virtual constraints makes the compliant hybrid zero dynamics actuated. Active force control is implemented within the HZD to create a virtual compliant element, allowing the effective leg stiffness to be varied throughout the gait. Stability analysis using the method of Poincaré is then carried out to check stability of the closed-loop system. The nominal periodic orbit is unstable and a linear event-based outer-loop controller is implemented to exponentially stabilize the running gait. Simulations demonstrate that the resulting closed-loop system is not adequately robust to perturbations in the knee angle at impact. For obtaining successful experiments, the robustness to perturbations needs to be improved and an additional nonlinear outer-loop controller is formulated based on insight from simplified models.

Next, before deploying the controller on the testbed, stretching in the cables that connect the pulleys of the transmission is addressed. Cable stretch is neither part of the control-oriented model nor part of the nominal control design. However severe cable stretch is present in the leg shape direction and the method of virtual compliance enables addressing this very easily. The stiffness of the virtual compliance is modified to account for cable stretch. This controller is implemented on MABEL with passive feet and with point feet to realize stable running motions. With the passive feet, running was realized at an average speed of 1.07 m/s, while with point feet, running was realized at an average speed of 1.95 m/s and a peak speed of 3.06 m/s. About 40% of the gait was spent in flight, with estimated peak ground clearance of 7 to 10 cms. Figure 1 illustrates a composite image of the running gait for MABEL.

The remainder of the paper is organized as follows. Section II presents a hybrid model for running that will be used for controller design. Section III gives a detailed presentation of the controller design for achieving exponentially stable running gaits. Next, with an eye towards successful experimental implementation, Section IV presents modifications to the controller design to address cable stretch along with details on an event-based outer-loop controller for increasing the robustness to perturbations in the knee angle at impact and to imperfections in the ground contact model. Section V describes the experiments performed to demonstrate the validity of the designed controller. Section VI discusses various aspects of the robot and the feedback controller that are revealed by the experiments. Finally Section VII provides concluding remarks.

II. CONTROL-ORIENTED MODEL FOR RUNNING

This section develops an appropriate mathematical model for the study of running. A hybrid model is developed, comprised of continuous phases representing the stance and flight phases of running, and discrete transitions between the two. Standard model hypotheses for a running gait and rigid impact as in (Westervelt et al., 2007, pp. 50-51) are assumed. In particular, the stance phase is a single support phase with one foot assumed pinned to the ground, while the flight phase has both feet above the ground. The stance to flight transition is usually a trivial lift map (Westervelt et al., 2007); however, for MABEL, due to the unilateral spring, this transition models an internal impact of the spring with a hardstop (see Figure 2(b)). The flight to stance transition models an instantaneous rigid impact, representing the impact of the swing toe with the ground. Both impact models are based on (Hurmuzlu and Marghitu, 1994).

This developed model will be employed for designing a controller to achieve exponentially stable running motions. Prior to experimental deployment, the designed controller will be validated on a higher-fidelity model (Park et al., 2011) that relaxes a few assumptions made here to closely represent the experimental testbed. Control design using the higher-fidelity model is not computationally feasible and further details regarding this are postponed to Section IV-B.

A. *MABEL's Unconstrained Dynamics*

The configuration space Q_{e} of the unconstrained dynamics of MABEL is a simply-connected subset of $\mathbb{S}^7 \times \mathbb{R}^2$: five DOF are associated with the links in the robot's body, two DOF are associated with the springs in series with the two leg-shape motors, and two DOF are associated with the horizontal and vertical position of the robot in the sagittal plane. A set of coordinates suitable for parametrization of the robot's linkage and transmission is $q_{\mathrm{e}} := (\ q_{\mathrm{LA}_{\mathrm{st}}};\ q_{\mathrm{mLS}_{\mathrm{st}}};\ q_{\mathrm{Bsp}_{\mathrm{st}}};\ q_{\mathrm{LA}_{\mathrm{sw}}};\ q_{\mathrm{mLS}_{\mathrm{sw}}};\ q_{\mathrm{Bsp}_{\mathrm{sw}}};\ q_{\mathrm{Tor}};\ p^h_{\mathrm{hip}};\ p^v_{\mathrm{hip}}\ )$, the subscripts st and sw refer to the stance and swing legs respectively. As in Figure 2, q_{Tor} is the torso angle, and $q_{\mathrm{LA}_{\mathrm{st}}}$, $q_{\mathrm{mLS}_{\mathrm{st}}}$, and $q_{\mathrm{Bsp}_{\mathrm{st}}}$ are the leg angle, leg-shape motor position, and $\mathrm{B}_{\mathrm{spring}}$ position, respectively for the stance leg. The swing leg variables, $q_{\mathrm{LA}_{\mathrm{sw}}}$, $q_{\mathrm{mLS}_{\mathrm{sw}}}$ and $q_{\mathrm{Bsp}_{\mathrm{sw}}}$ are defined similarly. For each leg, q_{LS} is determined from q_{mLS} and q_{Bsp} by

$$q_{LS} = 0.0318 q_{\mathrm{mLS}} + 0.193 q_{\mathrm{Bsp}}. \tag{1}$$

This relation reflects the fact that the cable differentials place the spring in series with the motor, with the pulleys introducing a gear ratio. The coordinates $p^h_{\mathrm{hip}}, p^v_{\mathrm{hip}}$ are the horizontal and vertical positions of the hip in the sagittal plane. The hip position is chosen as an independent coordinate instead of the center of mass because it was observed that this choice significantly reduces the number of terms in the symbolic expressions for the dynamics.

The equations of motion are obtained using the method of Lagrange. The Lagrangian for the unconstrained system, $\mathcal{L}_{\mathrm{e}} : TQ_{\mathrm{e}} \to \mathbb{R}$, is defined by

$$\mathcal{L}_{\mathrm{e}} = \mathcal{K}_{\mathrm{e}} - \mathcal{V}_{\mathrm{e}}, \tag{2}$$

where, $\mathcal{K}_{\mathrm{e}} : TQ_{\mathrm{e}} \to \mathbb{R}$ and $\mathcal{V}_{\mathrm{e}} : Q_{\mathrm{e}} \to \mathbb{R}$ are the total kinetic and potential energies of the mechanism, respectively. The total kinetic energy is obtained by summing the kinetic energy of the linkage, $\mathcal{K}^{link}_{\mathrm{e}}$, the kinetic energy of the stance and swing leg transmissions, $\mathcal{K}^{trans_{\mathrm{st}}}_{\mathrm{e}}, \mathcal{K}^{trans_{\mathrm{sw}}}_{\mathrm{e}}$, and the kinetic energy of the boom, $\mathcal{K}^{boom}_{\mathrm{e}}$,

$$\begin{aligned}\mathcal{K}_{\mathrm{e}}\left(q_{\mathrm{e}}, \dot{q}_{\mathrm{e}}\right) = \mathcal{K}^{link}_{\mathrm{e}}\left(q_{\mathrm{e}}, \dot{q}_{\mathrm{e}}\right) + \mathcal{K}^{trans_{\mathrm{st}}}_{\mathrm{e}}\left(q_{\mathrm{e}}, \dot{q}_{\mathrm{e}}\right) +\\ \mathcal{K}^{trans_{\mathrm{sw}}}_{\mathrm{e}}\left(q_{\mathrm{e}}, \dot{q}_{\mathrm{e}}\right) + \mathcal{K}^{boom}_{\mathrm{e}}\left(q_{\mathrm{e}}, \dot{q}_{\mathrm{e}}\right).\end{aligned} \tag{3}$$

The linkage model is standard. Physically, the boom constrains the robot to move on the surface of a sphere, and a full 3D model would be required to accurately model the robot and boom system. However, we assume the motion to be planar and, as in (Westervelt, 2003, p. 94), only consider the effects due to mass and inertia of the boom. This will introduce some discrepancies between simulation and experimental results. The symbolic expressions for the transmission model are available online at (Grizzle, 2010b).

Similar notation is used for the potential energy,

$$\begin{aligned}\mathcal{V}_{\mathrm{e}}\left(q_{\mathrm{e}}\right) = \mathcal{V}^{link}_{e}\left(q_{\mathrm{e}}\right) + \mathcal{V}^{trans_{\mathrm{st}}}_{\mathrm{e}}\left(q_{\mathrm{e}}\right) +\\ \mathcal{V}^{trans_{\mathrm{sw}}}_{\mathrm{e}}\left(q_{\mathrm{e}}\right) + \mathcal{V}^{boom}_{\mathrm{e}}.\end{aligned} \tag{4}$$

Due to its unilateral nature, the spring is not included in the potential energy of the transmission; only the mass of the motors and pulleys is included. The unilateral spring is considered as an external input to the system.

With the above considerations, the unconstrained robot dynamics can be determined through Lagrange's equations

$$\frac{d}{dt}\frac{\partial \mathcal{L}_{\mathrm{e}}}{\partial \dot{q}_{\mathrm{e}}} - \frac{\partial \mathcal{L}_{\mathrm{e}}}{\partial q_{\mathrm{e}}} = \Gamma_{\mathrm{e}}, \tag{5}$$

where, Γ_{e} is the vector of generalized forces acting on the robot and can be written as,

$$\begin{aligned}\Gamma_{\mathrm{e}} = {} & B_{\mathrm{e}} u + E_{\mathrm{ext}}\left(q_{\mathrm{e}}\right) F_{\mathrm{ext}} + \\ & B_{fric}\tau_{fric}\left(q_{\mathrm{e}}, \dot{q}_{\mathrm{e}}\right) + B_{sp}\tau_{sp}\left(q_{\mathrm{e}}, \dot{q}_{\mathrm{e}}\right),\end{aligned} \tag{6}$$

where the matrices B_{e}, E_{ext}, B_{fric}, and B_{sp} are derived from the principle of virtual work and define how the actuator torques u, the external forces F_{ext} at the leg, the joint friction forces τ_{fric}, and the spring torques τ_{sp} enter the model, respectively.

Applying Lagrange's equations (5), with the kinetic and potential energies defined by (3) and (4), respectively, results in the second-order dynamical model

$$D_{\mathrm{e}}\left(q_{\mathrm{e}}\right)\ddot{q}_{\mathrm{e}} + C_{\mathrm{e}}\left(q_{\mathrm{e}}, \dot{q}_{\mathrm{e}}\right)\dot{q}_{\mathrm{e}} + G_{\mathrm{e}}\left(q_{\mathrm{e}}\right) = \Gamma_{\mathrm{e}} \tag{7}$$

for the unconstrained dynamics of MABEL. Here D_{e} is the inertia matrix, the matrix C_{e} contains Coriolis and centrifugal terms, and G_{e} is the gravity vector.

B. MABEL's Constrained Dynamics

The model (7) can be particularized to describe the stance and flight dynamics by incorporating proper holonomic constraints. This results in lower degree of freedom models for the stance and flight phases.

1) Dynamics of Stance: For modeling the stance phase, the stance toe is assumed to act as a passive pivot joint (no slip, no rebound and no actuation). Hence, the Cartesian position of the hip, $\left(p^h_{\mathrm{hip}}, p^v_{\mathrm{hip}}\right)$, is defined by the coordinates of the stance leg and torso. The springs in the transmission are appropriately chosen to support the entire weight of the robot, and hence are stiff. Consequently, it is assumed that the spring on the swing leg does not deflect, that is, $q_{\mathrm{Bsp_{sw}}} \equiv 0$. It follows from (1) that $q_{\mathrm{mLS_{sw}}}$ and $q_{\mathrm{LS_{sw}}}$ are related by a gear ratio; $q_{\mathrm{mLS_{sw}}}$ is taken as the independent variable. With these assumptions, the generalized configuration variables in stance are taken as $q_{\mathrm{s}} := \left(q_{\mathrm{LA_{st}}}; q_{\mathrm{mLS_{st}}}; q_{\mathrm{Bsp_{st}}}; q_{\mathrm{LA_{sw}}}; q_{\mathrm{mLS_{sw}}}; q_{\mathrm{Tor}}\right)$.

The stance dynamics is obtained by applying the above holonomic constraints to the unconstrained dynamic model of Section II-A. The stance configuration space is therefore a co-dimension three submanifold of Q_{e}, i.e., $Q_{\mathrm{s}} := \left\{q_{\mathrm{e}} \in Q_{\mathrm{e}} \mid q_{\mathrm{Bsp_{sw}}} \equiv 0, p^h_{\mathrm{toe_{st}}} \equiv 0, p^v_{\mathrm{toe_{st}}} \equiv 0\right\}$. For later use, we denote by

$$q_{\mathrm{e}} = \Upsilon_{\mathrm{s}}\left(q_{\mathrm{s}}\right) \tag{8}$$

the value of q_{e} when $q_{\mathrm{s}} \in Q_{\mathrm{s}}$, and by

$$q_{\mathrm{s}} = \Pi_{\mathrm{s}}\left(q_{\mathrm{e}}\right) \tag{9}$$

the value of q_{e} projected onto $Q_{\mathrm{s}} \subset Q_{\mathrm{e}}$, such that, $\Pi_{\mathrm{s}} \circ \Upsilon_{\mathrm{s}} = id_{Q_{\mathrm{s}}}$ as suggested by the commutative diagram of Figure 3. Further, the unconstrained velocity $\dot{q}_{\mathrm{e}}$ can be obtained from the stance velocity $\dot{q}_{\mathrm{s}}$ through the differential of the map Υ_{s} at the point $q_{\mathrm{s}} \in Q_{\mathrm{s}}$, i.e.,

$$\begin{tikzcd}
\dot{q}_{\mathrm{s}} \in T_{q_{\mathrm{s}}}Q_{\mathrm{s}} \arrow[rr, "id_{T_{q_{\mathrm{s}}}Q_{\mathrm{s}}}"] \arrow[dr, "(D\Upsilon_{\mathrm{s}})_{q_{\mathrm{s}}}"'] & \text{(fiber)} & \dot{q}_{\mathrm{s}} \in T_{q_{\mathrm{s}}}Q_{\mathrm{s}} \\
& \dot{q}_{\mathrm{e}} \in T_{\Upsilon_{\mathrm{s}}(q_{\mathrm{s}}))}Q_{\mathrm{e}} \arrow[ur, "(D\Pi_{\mathrm{s}})_{\Upsilon_{\mathrm{s}}(q_{\mathrm{s}})}"'] &
\end{tikzcd}$$

(a)

$$\begin{tikzcd}
q_{\mathrm{s}} \in Q_{\mathrm{s}} \arrow[rr, "id_{Q_{\mathrm{s}}}"] \arrow[dr, "\Upsilon_{\mathrm{s}}"'] & \text{(base)} & q_{\mathrm{s}} \in Q_{\mathrm{s}} \\
& q_{\mathrm{e}} \in Q_{\mathrm{e}} \arrow[ur, "\Pi_{\mathrm{s}}"'] &
\end{tikzcd}$$

(b)

Fig. 3. The commutative diagram between the state spaces for the constrained stance dynamics and the unconstrained dynamics is shown. A similar diagram exists for the state space of the flight dynamics. This is not shown here, but is easily obtained by replacing all the subscripts for the stance phase with those of the flight phase.

$$\dot{q}_{\mathrm{e}} = \left(D\Upsilon_{\mathrm{s}}\right)_{q_{\mathrm{s}}}\left(\dot{q}_{\mathrm{s}}\right), \tag{10}$$

where $\left(D\Upsilon_{\mathrm{s}}\right)_{q_{\mathrm{s}}} : T_{q_{\mathrm{s}}}Q_{\mathrm{s}} \to T_{\Upsilon_{\mathrm{s}}(q_{\mathrm{s}})}Q_{\mathrm{e}}$. Similarly, the stance velocity can be obtained from the unconstrained velocity through the differential of the map Π_{s} at the point $q_{\mathrm{e}} \in Q_{\mathrm{e}}$, i.e.,

$$\dot{q}_{\mathrm{s}} = \left(D\Pi_{\mathrm{s}}\right)_{q_{\mathrm{e}}}\left(\dot{q}_{\mathrm{e}}\right), \tag{11}$$

where $\left(D\Pi_{\mathrm{s}}\right)_{q_{\mathrm{s}}} : T_{q_{\mathrm{e}}}Q_{\mathrm{e}} \to T_{\Pi_{\mathrm{s}}(q_{\mathrm{e}})}Q_{\mathrm{s}}$. Moreover, $\left(D\Pi_{\mathrm{s}}\right)_{\Upsilon_{\mathrm{s}}(q_{\mathrm{s}})} \circ \left(D\Upsilon_{\mathrm{s}}\right)_{q_{\mathrm{s}}} = id_{T_{q_{\mathrm{s}}}Q_{\mathrm{s}}}$.

The resulting constrained Lagrangian $\mathcal{L}_{\mathrm{s}} : TQ_{\mathrm{s}} \to \mathbb{R}$ can be expressed as

$$\mathcal{L}_{\mathrm{s}} := \mathcal{L}_{\mathrm{e}}\left(q_{\mathrm{e}}, \dot{q}_{\mathrm{e}}\right)|_{\left\{q_{\mathrm{Bsp_{sw}}} \equiv 0, p^h_{\mathrm{toe_{st}}} \equiv 0, p^v_{\mathrm{toe_{st}}} \equiv 0\right\}}, \tag{12}$$

and the dynamics of stance are obtained through Lagrange's equations, expressed in standard form as

$$D_{\mathrm{s}}\left(q_{\mathrm{s}}\right)\ddot{q}_{\mathrm{s}} + C_{\mathrm{s}}\left(q_{\mathrm{s}}, \dot{q}_{\mathrm{s}}\right)\dot{q}_{\mathrm{s}} + G_{\mathrm{s}}\left(q_{\mathrm{s}}\right) = \Gamma_{\mathrm{s}}, \tag{13}$$

where, $\Gamma_{\mathrm{s}} := B_{\mathrm{s}} u + B_{fric}\tau_{fric}\left(q_{\mathrm{s}}, \dot{q}_{\mathrm{s}}\right) + B_{sp}\tau_{sp}\left(q_{\mathrm{s}}, \dot{q}_{\mathrm{s}}\right)$ is the vector of generalized forces acting on the robot.

The state-space form of the stance dynamics, with the state vector $x_{\mathrm{s}} := (q_{\mathrm{s}}; \dot{q}_{\mathrm{s}}) \in TQ_{\mathrm{s}}$, can be expressed as,

$$\begin{aligned}\dot{x}_{\mathrm{s}} := \begin{bmatrix}\dot{q}_{\mathrm{s}} \\ \ddot{q}_{\mathrm{s}}\end{bmatrix} &= \begin{bmatrix}\dot{q}_{\mathrm{s}} \\ -D_{\mathrm{s}}^{-1}H_{\mathrm{s}}\end{bmatrix} + \begin{bmatrix}0 \\ D_{\mathrm{s}}^{-1}B_{\mathrm{s}}\end{bmatrix} u \\ &=: f_{\mathrm{s}}(x_{\mathrm{s}}) + g_{\mathrm{s}}(x_{\mathrm{s}})u,\end{aligned} \tag{14}$$

where, $f_{\mathrm{s}}, g_{\mathrm{s}}$ are the drift and input vector fields for the stance dynamics, and $H_{\mathrm{s}} := C_{\mathrm{s}}\left(q_{\mathrm{s}}, \dot{q}_{\mathrm{s}}\right)\dot{q}_{\mathrm{s}} + G_{\mathrm{s}}\left(q_{\mathrm{s}}\right) - B_{fric}\tau_{fric}\left(q_{\mathrm{s}}, \dot{q}_{\mathrm{s}}\right) - B_{sp}\tau_{sp}\left(q_{\mathrm{s}}, \dot{q}_{\mathrm{s}}\right)$.

2) Dynamics of Flight: In the flight phase, both the feet are off the ground, and the robot's center of mass follows a ballistic motion under the influence of gravity. Thus the flight dynamics can be modeled by the unconstrained dynamics developed in the previous section. Further, for reasons mentioned for the swing leg during the stance phase, and the fact that neither leg is in contact with the ground during the flight phase, it will be assumed that the springs on each leg do not deflect during the flight phase. Therefore, $q_{\mathrm{Bsp_{st}}} \equiv 0, q_{\mathrm{Bsp_{sw}}} \equiv 0$. This assumption is computationally advantageous since it eliminates the stiffness in the model while integrating the differential equations. Thus, the configuration space of the flight dynamics is a co-dimension two submanifold of Q_{e}, i.e., $Q_{\mathrm{f}} := \left\{q_{\mathrm{e}} \in Q_{\mathrm{e}} \mid q_{\mathrm{Bsp_{st}}} \equiv 0, q_{\mathrm{Bsp_{sw}}} \equiv 0\right\}$. It follows that, the generalized configuration variables in the flight phase can be taken as $q_{\mathrm{f}} := \left(q_{\mathrm{LA_{st}}}; q_{\mathrm{mLS_{st}}}; q_{\mathrm{LA_{sw}}}; q_{\mathrm{mLS_{sw}}}; q_{\mathrm{Tor}}; p^h_{\mathrm{hip}}; p^v_{\mathrm{hip}}\right)$. For later use, we denote by

$$q_{\mathrm{e}} = \Upsilon_{\mathrm{f}}\left(q_{\mathrm{f}}\right), \tag{15}$$

the value of q_{e} when $q_{\mathrm{f}} \in Q_{\mathrm{f}}$, and

$$q_{\mathrm{f}} = \Pi_{\mathrm{f}}\left(q_{\mathrm{e}}\right), \tag{16}$$

the value of q_{e} projected onto $Q_{\mathrm{f}} \subset Q_{\mathrm{e}}$, such that, $\Pi_{\mathrm{f}} \circ \Upsilon_{\mathrm{f}} = id_{Q_{\mathrm{f}}}$ as suggested by the commutative diagram of Figure 3 after replacing the subscripts for the stance phase with those of the flight phase. Further, the unconstrained velocity $\dot{q}_{\mathrm{e}}$ can be obtained from the flight velocity $\dot{q}_{\mathrm{f}}$ through the differential of the map Υ_{f} at the point $q_{\mathrm{f}} \in Q_{\mathrm{f}}$, i.e.,

$$\dot{q}_{\mathrm{e}} = \left(D\Upsilon_{\mathrm{f}}\right)_{q_{\mathrm{f}}}\left(\dot{q}_{\mathrm{f}}\right), \tag{17}$$

where $\left(D\Upsilon_{\mathrm{f}}\right)_{q_{\mathrm{f}}} : T_{q_{\mathrm{f}}}Q_{\mathrm{f}} \to T_{\Upsilon_{\mathrm{f}}(q_{\mathrm{f}})}Q_{\mathrm{e}}$. Similarly, the stance velocity can be obtained from the unconstrained velocity through the differential of the map Π_{f} at the point $q_{\mathrm{e}} \in Q_{\mathrm{e}}$, i.e.,

$$\dot{q}_{\mathrm{f}} = \left(D\Pi_{\mathrm{f}}\right)_{q_{\mathrm{e}}}\left(\dot{q}_{\mathrm{e}}\right), \tag{18}$$

where $\left(D\Pi_{\mathrm{f}}\right)_{q_{\mathrm{f}}} : T_{q_{\mathrm{e}}}Q_{\mathrm{e}} \to T_{\Pi_{\mathrm{f}}(q_{\mathrm{e}})}Q_{\mathrm{f}}$. Moreover, $\left(D\Pi_{\mathrm{f}}\right)_{\Upsilon_{\mathrm{f}}(q_{\mathrm{f}})} \circ \left(D\Upsilon_{\mathrm{f}}\right)_{q_{\mathrm{f}}} = \mathrm{id}_{T_{q_{\mathrm{f}}}Q_{\mathrm{f}}}$.

Thus, the resulting Lagrangian $\mathcal{L}_{\mathrm{f}} : TQ_{\mathrm{f}} \to \mathbb{R}$ in the flight phase can be expressed as

$$\mathcal{L}_{\mathrm{f}}\left(q_{\mathrm{f}}, \dot{q}_{\mathrm{f}}\right) = \mathcal{L}_{\mathrm{e}}\left(q_{\mathrm{e}}, \dot{q}_{\mathrm{e}}\right)|_{q_{\mathrm{Bsp_{st}}} \equiv 0, q_{\mathrm{Bsp_{sw}}} \equiv 0}, \tag{19}$$

and the flight dynamics can be expressed in the standard form as

$$D_{\mathrm{f}}\left(q_{\mathrm{f}}\right)\ddot{q}_{\mathrm{f}} + C_{\mathrm{f}}\left(q_{\mathrm{f}}, \dot{q}_{\mathrm{f}}\right)\dot{q}_{\mathrm{f}} + G_{\mathrm{f}}\left(q_{\mathrm{f}}\right) = \Gamma_{\mathrm{f}}, \tag{20}$$

where, $\Gamma_{\mathrm{f}} := B_{\mathrm{f}}u + B_{fric}\tau_{fric}\left(q_{\mathrm{f}}, \dot{q}_{\mathrm{f}}\right) + B_{sp}\tau_{sp}\left(q_{\mathrm{f}}, \dot{q}_{\mathrm{f}}\right)$ is the vector of generalized forces acting on the robot.

The state-space form of the flight dynamics, with the state vector $x_{\mathrm{f}} := (q_{\mathrm{f}}; \dot{q}_{\mathrm{f}}) \in TQ_{\mathrm{f}}$, can be expressed as,

$$\begin{aligned} \dot{x}_{\mathrm{f}} := \begin{bmatrix} q_{\mathrm{f}} \\ \dot{q}_{\mathrm{f}} \end{bmatrix} &= \begin{bmatrix} \dot{q}_{\mathrm{f}} \\ -D_{\mathrm{f}}^{-1}H_{\mathrm{f}} \end{bmatrix} + \begin{bmatrix} 0 \\ D_{\mathrm{f}}^{-1}B_{\mathrm{f}} \end{bmatrix} u \\ &=: f_{\mathrm{f}}(x_{\mathrm{f}}) + g_{\mathrm{f}}(x_{\mathrm{f}})u \end{aligned} \tag{21}$$

where, $f_{\mathrm{f}}, g_{\mathrm{f}}$ are the drift and input vector fields for the flight dynamics, and $H_{\mathrm{f}} = C_{\mathrm{f}}\left(q_{\mathrm{f}}, \dot{q}_{\mathrm{f}}\right)\dot{q}_{\mathrm{f}} + G_{\mathrm{f}}\left(q_{\mathrm{f}}\right) - B_{fric}\tau_{fric}\left(q_{\mathrm{f}}, \dot{q}_{\mathrm{f}}\right) - B_{sp}\tau_{sp}\left(q_{\mathrm{f}}, \dot{q}_{\mathrm{f}}\right)$.

C. MABEL's Transitions

1) Stance to Flight Transition Map: Physically, the robot takes off when the normal component of the ground reaction force acting on the stance toe, $F^N_{toe_{\mathrm{st}}}$, becomes zero. The ground reaction force at the stance toe can be computed as a function of the acceleration of the COM and thus depends on the inputs $u \in \mathcal{U}$ of the system described by (14). To formally express the takeoff event, we first define a trivial fiber bundle,

$$\pi : B \to TQ_{\mathrm{s}}, \tag{22}$$

where $B = TQ_{\mathrm{s}} \times \mathcal{U}$. Mathematically, takeoff occurs when the solution of (14) intersects the co-dimension one switching manifold $\mathcal{S}_{\mathrm{s}\to\mathrm{f}}$ in the fiber bundle (22), defined as,

$$\mathcal{S}_{\mathrm{s}\to\mathrm{f}} := \left\{(x_{\mathrm{s}}, u) \in TQ_{\mathrm{s}} \times \mathcal{U} \mid H_{\mathrm{s}\to\mathrm{f}}(x_{\mathrm{s}}, u) = 0\right\}, \tag{23}$$

where the threshold function $H_{\mathrm{s}\to\mathrm{f}} : TQ_{\mathrm{s}} \times \mathcal{U} \to \mathbb{R}$ is defined as $H_{\mathrm{s}\to\mathrm{f}}(x_{\mathrm{s}}, u) = F^N_{toe_{\mathrm{st}}}$, with $F^N_{toe_{\mathrm{st}}}$ being the normal component of the ground reaction force at the stance foot.

The stance to flight transition map, $\Delta_{\mathrm{s}\to\mathrm{f}} : \mathcal{S}_{\mathrm{s}\to\mathrm{f}} \to TQ_{\mathrm{f}}$, is defined as

$$\Delta_{\mathrm{s}\to\mathrm{f}}\left(x^-_{\mathrm{s}}, u^-\right) := \begin{bmatrix} \Delta^q_{\mathrm{s}\to\mathrm{f}}(q^-_{\mathrm{s}}) \\ (\Delta^{\dot{q}}_{\mathrm{s}\to\mathrm{f}})_{q^-_{\mathrm{s}}}(\dot{q}^-_{\mathrm{s}}, u^-) \end{bmatrix}, \tag{24}$$

where, $x^-_{\mathrm{s}} = (q^-_{\mathrm{s}}; \dot{q}^-_{\mathrm{s}}) \in TQ_{\mathrm{s}}$ is the final state of the stance phase and $u^- \in \mathcal{U}$ is the input at this instant. The base and fiber components, $\Delta^q_{\mathrm{s}\to\mathrm{f}} : Q_{\mathrm{s}} \to Q_{\mathrm{f}}$, $(\Delta^{\dot{q}}_{\mathrm{s}\to\mathrm{f}})_{q_{\mathrm{s}}} : T_{q_{\mathrm{s}}}Q_{\mathrm{s}} \times \mathcal{U} \to T_{\Delta^q_{\mathrm{s}\to\mathrm{f}}(q_{\mathrm{s}})}Q_{\mathrm{f}}$ define the transition maps for the configuration variables and their velocities, respectively. The initial state of the flight phase, $x^+_{\mathrm{f}} \in TQ_{\mathrm{f}}$, is the post transition state and is obtained as,

$$x^+_{\mathrm{f}} = \Delta_{\mathrm{s}\to\mathrm{f}}\left(x^-_{\mathrm{s}}, u^-\right). \tag{25}$$

On transition from the stance to flight phase, the stance leg comes off the ground and takeoff occurs. The linkage joint angles do not change over this instantaneous transition. During the stance phase, the spring is compressed. When the stance leg comes off the ground, the spring rapidly decompresses until it reaches its rest position. At this instant, there is an impact of the pulley $\mathrm{B_{spring}}$ hitting the hard stop. Mathematically, this is captured by the impact map $\Delta_{Stp} : TQ_{\mathrm{e}} \to TQ_{\mathrm{e}}$ representing the impact with the hard stop. The base and fiber components of the stance to flight transition map can then be expressed using the impact map as,

$$\Delta^q_{\mathrm{s}\to\mathrm{f}} = \Pi_{\mathrm{f}} \circ \Delta^q_{Stp} \circ \Upsilon_{\mathrm{s}}, \tag{26}$$

$$\begin{aligned} (\Delta^{\dot{q}}_{\mathrm{s}\to\mathrm{f}})_{q^-_{\mathrm{s}}} =& (D\Pi_{\mathrm{f}})_{\Delta^q_{Stp} \circ \Upsilon_{\mathrm{s}}(q^-_{\mathrm{s}})} \circ (\Delta^{\dot{q}}_{Stp})_{\Upsilon_{\mathrm{s}}(q^-_{\mathrm{s}})} \circ \\ & (D\Upsilon_{\mathrm{s}})_{q^-_{\mathrm{s}}} \circ \pi, \end{aligned} \tag{27}$$

such that diagram of Figure 4 commutes. Υ_{s}, Π_{f} are as in (8), (16) respectively, and π is as defined in (22).

$$\begin{tikzcd}
q_{\mathrm{s}}^{-} \in Q_{\mathrm{s}} \arrow[r, "\Delta_{\mathrm{s}\to\mathrm{f}}^{q}"] \arrow[d, "\Upsilon_{\mathrm{s}}"'] \arrow[dr, phantom, "\text{(base)}"] & q_{\mathrm{f}}^{+} \in Q_{\mathrm{f}} \\
q_{\mathrm{e}}^{-} \in Q_{\mathrm{e}} \arrow[r, "\Delta_{Stp}^{q} = \Pi_{\mathrm{Bsp}}"'] & q_{\mathrm{e}}^{+} \in Q_{\mathrm{e}} \arrow[u, "\Pi_{\mathrm{f}}"']
\end{tikzcd}$$

(a)

$$\begin{tikzcd}
(\dot{q}_{\mathrm{s}}^{-}, u) \in T_{q_{\mathrm{s}}^{-}} Q_{\mathrm{s}} \times \mathcal{U} \arrow[r, "(\Delta_{\mathrm{s}\to\mathrm{f}}^{\dot{q}})_{q_{\mathrm{s}}^{-}}"] \arrow[d, "(D\Upsilon_{\mathrm{s}})_{q_{\mathrm{s}}^{-}} \circ \pi"'] \arrow[dr, phantom, "\text{(fiber)}"] & \dot{q}_{\mathrm{f}}^{+} \in T_{\Delta_{\mathrm{s}\to\mathrm{f}}^{q}(q_{\mathrm{s}}^{-})} Q_{\mathrm{f}} \\
\dot{q}_{\mathrm{e}}^{-} \in T_{\Upsilon_{\mathrm{s}}(q_{\mathrm{s}}^{-})} Q_{\mathrm{e}} \arrow[r, "(\Delta_{Stp}^{\dot{q}})_{\Upsilon_{\mathrm{s}}(q_{\mathrm{s}}^{-})}"'] & \dot{q}_{\mathrm{e}}^{+} \in T_{\Delta_{Stp}^{q} \circ \Upsilon_{\mathrm{s}}(q_{\mathrm{s}}^{-})} Q_{\mathrm{e}} \arrow[u, "(D\Pi_{\mathrm{f}})_{\Delta_{Stp}^{q} \circ \Upsilon_{\mathrm{s}}(q_{\mathrm{s}}^{-})}"']
\end{tikzcd}$$

(b)

Fig. 4. Commutative diagrams for obtaining the (a) base, and (b) fiber components of the stance to flight transition map.

The rest of this section will focus on deriving the base and fiber components of the impact map Δ_{Stp}.

As per earlier discussions, the impact of the pulley $\mathrm{B}_{\mathrm{spring}}$ with the hard stop requires a change in the position of the transmission variable (specifically $q_{\mathrm{mLS}_{\mathrm{st}}}$) such that the linkage positions are invariant. Thus the impact map for the coordinates can be expressed as

$$\Delta_{Stp}^{q} := \Pi_{\mathrm{Bsp}}, \tag{28}$$

where Π_{Bsp} is a projection from Q_{e} onto the co-dimension two submanifold $\{q_{\mathrm{e}} \in Q_{\mathrm{e}} \mid q_{\mathrm{Bsp}_{\mathrm{st}}} \equiv 0, q_{\mathrm{Bsp}_{\mathrm{sw}}} \equiv 0\}$ such that the linkage coordinates $(q_{\mathrm{LA}}, q_{\mathrm{LS}}, q_{\mathrm{Tor}})$ remain invariant under the projection. Thus Π_{Bsp} resets the spring to its rest position by modifying the leg-shape motor position such that the leg-shape position itself is unchanged.

Next, the impact map for the velocities is derived as follows. Let τ_R to be the impulsive torque being applied at the pulley $\mathrm{B}_{\mathrm{spring}}$ due to the stopper. Then the generalized external impulsive force acting on the system is obtained from the principle of virtual work as,

$$F_{\mathrm{ext}} = \frac{\partial q_{\mathrm{Bsp}_{\mathrm{st}}}}{\partial q_{\mathrm{e}}}^{\mathrm{T}} \tau_R. \tag{29}$$

We have two constraints that need to be satisfied. The first condition is the trivial post impact velocity of the spring on the stance leg to be zero. The second condition is obtained by integrating the unconstrained dynamics, (7), over the duration of the instantaneous event. These conditions then are,

$$\dot{q}_{\mathrm{Bsp}_{\mathrm{st}}}^{+} = 0 \implies \frac{\partial q_{\mathrm{Bsp}_{\mathrm{st}}}}{\partial q_{\mathrm{e}}} \dot{q}_{\mathrm{e}}^{+} = 0. \tag{30}$$

$$D_{\mathrm{e}}\left(q_{\mathrm{e}}^{+}\right) \dot{q}_{\mathrm{e}}^{+} - D_{\mathrm{e}}\left(q_{\mathrm{e}}^{-}\right) \dot{q}_{\mathrm{e}}^{-} = F_{\mathrm{ext}}, \tag{31}$$

From (29)-(31), assembling the constraints and solving for the post-impact velocity, we obtain the map,

$$\left(\Delta_{Stp}^{\dot{q}}\right)_{q_{\mathrm{e}}^{-}} \left(\dot{q}_{\mathrm{e}}^{-}\right) = \begin{bmatrix} I & 0 \end{bmatrix} A_{\mathrm{s}\to\mathrm{f}}^{-1} \, B_{\mathrm{s}\to\mathrm{f}} \tag{32}$$

where,

$$A_{\mathrm{s}\to\mathrm{f}} = \begin{bmatrix} \frac{\partial q_{\mathrm{Bsp}_{\mathrm{st}}}}{\partial q_{\mathrm{e}}} & 0 \\ D_{\mathrm{e}}\left(\Delta_{Stp}^{q}(q_{\mathrm{e}}^{-})\right) & -\frac{\partial q_{\mathrm{Bsp}_{\mathrm{st}}}}{\partial q_{\mathrm{e}}}^{\mathrm{T}} \end{bmatrix}, \tag{33}$$

$$B_{\mathrm{s}\to\mathrm{f}} = \begin{bmatrix} 0 \\ D_{\mathrm{e}}\left(q_{\mathrm{e}}^{-}\right) \dot{q}_{\mathrm{e}}^{-} \end{bmatrix}, \tag{34}$$

and Δ_{Stp}^{q} is as defined in (28). With this, the base and fiber components of the stance to flight transition map, (24), are completely defined.

2) Flight to Stance Transition Map: The robot physically transitions from flight phase to stance phase when the swing toe contacts the ground surface. It is assumed that there is no rebound or slipping when this contact occurs. Thus, mathematically, this transition occurs when the solution of (21) intersects the co-dimension one switching manifold defined as,

$$\mathcal{S}_{\mathrm{f}\to\mathrm{s}} := \left\{x_{\mathrm{f}} \in TQ_{\mathrm{f}} \mid H_{\mathrm{f}\to\mathrm{s}}(x_{\mathrm{f}}) = 0\right\}, \tag{35}$$

where the threshold function $H_{\mathrm{f}\to\mathrm{s}} : TQ_{\mathrm{f}\to\mathrm{s}} \to \mathbb{R}$ is defined as $H_{\mathrm{f}\to\mathrm{s}}(x_{\mathrm{f}}) = p_{\mathrm{toe}_{\mathrm{sw}}}^{v}$, with $p_{\mathrm{toe}_{\mathrm{sw}}}^{v}$ being the vertical component of the swing toe.

The flight to stance transition map, $\Delta_{\mathrm{f}\to\mathrm{s}} : \mathcal{S}_{\mathrm{f}\to\mathrm{s}} \to TQ_{\mathrm{s}}$, is defined as

$$\Delta_{\mathrm{f}\to\mathrm{s}}\left(x_{\mathrm{f}}^{-}\right) := \begin{bmatrix} \Delta_{\mathrm{f}\to\mathrm{s}}^{q}(q_{\mathrm{f}}^{-}) \\ (\Delta_{\mathrm{f}\to\mathrm{s}}^{\dot{q}})_{q_{\mathrm{f}}^{-}}(\dot{q}_{\mathrm{f}}^{-}) \end{bmatrix}, \tag{36}$$

where, $x_{\mathrm{f}}^{-} = \left(q_{\mathrm{f}}^{-}; \dot{q}_{\mathrm{f}}^{-}\right) \in TQ_{\mathrm{f}}$ is the final state of the flight phase. The base and fiber components, $\Delta_{\mathrm{f}\to\mathrm{s}}^{q} : Q_{\mathrm{f}} \to Q_{\mathrm{s}}$, $(\Delta_{\mathrm{f}\to\mathrm{s}}^{\dot{q}})_{q_{\mathrm{f}}} : T_{q_{\mathrm{f}}}Q_{\mathrm{f}} \to T_{\Delta_{\mathrm{f}\to\mathrm{s}}^{q}(q_{\mathrm{f}})}Q_{\mathrm{s}}$ define the transition maps for the configuration variables and their velocities, respectively. The initial state of the stance phase, $x_{\mathrm{s}}^{+} \in TQ_{\mathrm{s}}$, is the post impact state and is obtained as,

$$x_{\mathrm{s}}^{+} = \Delta_{\mathrm{f}\to\mathrm{s}}\left(x_{\mathrm{f}}^{-}\right). \tag{37}$$

The impact being modeled here is that of the swing leg impacting the ground. Mathematically, this is captured by the impact map $\Delta_{Gnd} : TQ_{\mathrm{e}} \to TQ_{\mathrm{e}}$ representing the impact with the ground. The base and fiber components of the flight to stance transition map can then be expressed using the impact map as,

$$\Delta_{\mathrm{f}\to\mathrm{s}}^{q} = \Pi_{\mathrm{s}} \circ R \circ \Delta_{Gnd}^{q} \circ \Upsilon_{\mathrm{f}}, \tag{38}$$

$$\begin{aligned}(\Delta_{\mathrm{f}\to\mathrm{s}}^{\dot{q}})_{q_{\mathrm{f}}^{-}} = & (D\Pi_{\mathrm{s}})_{\Delta_{Gnd}^{q} \circ \Upsilon_{\mathrm{f}}(q_{\mathrm{f}}^{-})} \circ R \circ \\ & (\Delta_{Gnd}^{\dot{q}})_{\Upsilon_{\mathrm{f}}(q_{\mathrm{f}}^{-})} \circ (D\Upsilon_{\mathrm{f}})_{q_{\mathrm{f}}^{-}},\end{aligned} \tag{39}$$

such that diagram of Figure 5 commutes. Υ_{f}, Π_{s} are as in (15), (9) respectively, and R is a linear operator representing coordinate relabeling as found in (Westervelt et al., 2007, p. 57).

$$\begin{tikzcd}
q_{\mathrm{f}}^- \in Q_{\mathrm{f}} \arrow[r, "\Delta^q_{\mathrm{f}\to\mathrm{s}}"] \arrow[d, "\Upsilon_{\mathrm{f}}"'] \arrow[dr, phantom, "\text{(base)}"] & q_{\mathrm{s}}^+ \in Q_{\mathrm{s}} \\
q_{\mathrm{e}}^- \in Q_{\mathrm{e}} \arrow[r, "\Delta^q_{Gnd} = \mathrm{id}_{Q_{\mathrm{e}}}"'] & q_{\mathrm{e}}^+ \in Q_{\mathrm{e}} \arrow[u, "\Pi_{\mathrm{s}} \circ R"']
\end{tikzcd}$$

(a)

$$\begin{tikzcd}
\dot{q}_{\mathrm{f}}^- \in T_{q_{\mathrm{f}}^-} Q_{\mathrm{f}} \arrow[r, "(\Delta^{\dot{q}}_{\mathrm{f}\to\mathrm{s}})_{q_{\mathrm{f}}^-}"] \arrow[d, "(D\Upsilon_{\mathrm{f}})_{q_{\mathrm{f}}^-}"'] \arrow[dr, phantom, "\text{(fiber)}"] & \dot{q}_{\mathrm{s}}^+ \in T_{\Delta^q_{\mathrm{f}\to\mathrm{s}}(q_{\mathrm{f}}^-)} Q_{\mathrm{s}} \\
\dot{q}_{\mathrm{e}}^- \in T_{\Upsilon_{\mathrm{f}}(q_{\mathrm{f}}^-)} Q_{\mathrm{e}} \arrow[r, "(\Delta^{\dot{q}}_{Gnd})_{\Upsilon_{\mathrm{f}}(q_{\mathrm{f}}^-)}"'] & \dot{q}_{\mathrm{e}}^+ \in T_{\Delta^q_{Gnd} \circ \Upsilon_{\mathrm{f}}(q_{\mathrm{f}}^-)} Q_{\mathrm{e}} \arrow[u, "(D\Pi_{\mathrm{s}})_{\Delta^q_{Gnd} \circ \Upsilon_{\mathrm{f}}(q_{\mathrm{f}}^-)} \circ R"']
\end{tikzcd}$$

(b)

Fig. 5. Commutative diagrams for obtaining the (a) base, and (b) fiber components of the flight to stance transition map.

The rest of this section will focus on deriving the base and fiber components of the impact map Δ_{Gnd}.

The instantaneous impact with the ground does not result in a change in the linkage positions. Further since both legs are off the ground, the springs are at their rest positions and thus the position of the transmission variables are invariant under this impact. Thus the impact map for the coordinates can be expressed as

$$\Delta^q_{Gnd} := \mathrm{id}_{Q_{\mathrm{e}}}. \tag{40}$$

Next, the impact map for the velocities is derived as follows. Let I_R to be the impulsive force on the foot due to the ground-foot impact. Furthermore let τ_R be the constraint torque at the pulley $\mathrm{B}_{\mathrm{spring}}$ to maintain the spring at its rest position (This is not an impact torque, but just a torque required to continue to enforce the constraint). Then the generalized external impulsive force acting on the system is obtained from the principle of virtual work as,

$$F_{\mathrm{ext}} = \frac{\partial p_{\mathrm{toe_{sw}}}}{\partial q_{\mathrm{e}}}^{\mathrm{T}} I_R + \left(\frac{\partial q_{\mathrm{Bsp_{st}}}}{\partial q_{\mathrm{e}}}\right)^{\mathrm{T}} \tau_R. \tag{41}$$

We have three constraints that need to be satisfied at impact. The first condition is for the new swing leg to have zero spring velocity. The second condition is for the new stance toe to have zero velocity. The third constraint is obtained by integrating the unconstrained dynamics, (7), over the duration of the instantaneous event. These conditions then are,

$$\dot{q}^+_{\mathrm{Bsp_{st}}} = 0 \implies \frac{\partial q_{\mathrm{Bsp_{st}}}}{\partial q_{\mathrm{e}}} \dot{q}_{\mathrm{e}}^+ = 0. \tag{42}$$

$$\dot{p}^+_{\mathrm{toe_{sw}}} = 0 \implies \frac{\partial p_{\mathrm{toe_{sw}}}}{\partial q_{\mathrm{e}}} \dot{q}_{\mathrm{e}}^+ = 0, \tag{43}$$

$$D_{\mathrm{e}}\left(q_{\mathrm{e}}^+\right) \dot{q}_{\mathrm{e}}^+ - D_{\mathrm{e}}\left(q_{\mathrm{e}}^-\right) \dot{q}_{\mathrm{e}}^- = F_{\mathrm{ext}}, \tag{44}$$

From (41)-(44), assembling the constraints and solving for the post-impact velocity, we obtain the map,

$$\left(\Delta^{\dot{q}}_{Gnd}\right)_{q_{\mathrm{e}}^-} \left(\dot{q}_{\mathrm{e}}^-\right) = \begin{bmatrix} I & 0 & 0 \end{bmatrix} A^{-1}_{\mathrm{f}\to\mathrm{s}} \, B_{\mathrm{f}\to\mathrm{s}}, \tag{45}$$

where,

$$A_{\mathrm{f}\to\mathrm{s}} = \begin{bmatrix} \frac{\partial q_{\mathrm{Bsp_{st}}}}{\partial q_{\mathrm{e}}} & 0 & 0 \\ \frac{\partial p_{\mathrm{toe_{sw}}}}{\partial q_{\mathrm{e}}} & 0 & 0 \\ D_{\mathrm{e}}(\Delta^q_{Gnd}(q_{\mathrm{e}}^-)) & -\frac{\partial p_{\mathrm{toe_{sw}}}}{\partial q_{\mathrm{e}}}^{\mathrm{T}} & -\frac{\partial p_{\mathrm{Bsp_{st}}}}{\partial q_{\mathrm{e}}}^{\mathrm{T}} \end{bmatrix}, \tag{46}$$

$$B_{\mathrm{f}\to\mathrm{s}} = \begin{bmatrix} 0 \\ 0 \\ D_{\mathrm{e}}\left(q_{\mathrm{e}}^-\right) \dot{q}_{\mathrm{e}}^- \end{bmatrix}, \tag{47}$$

and Δ^q_{Gnd} is as defined in (40). With this, the base and fiber components of the flight to stance transition map, (36), are completely defined.

D. Hybrid Model of Running

The hybrid model of running is based on the dynamics developed in Sections II-B1, II-B2, and transition maps derived in Sections II-C1, II-C2. The continuous dynamics with discrete state transitions between the stance and flight phases is represented as,

$$\Sigma_{\mathrm{s}} : \begin{cases} \dot{x}_{\mathrm{s}} = f_{\mathrm{s}}\left(x_{\mathrm{s}}\right) + g_{\mathrm{s}}\left(x_{\mathrm{s}}\right) u, & \left(x_{\mathrm{s}}^-, u^-\right) \notin S_{\mathrm{s}\to\mathrm{f}} \\ x_{\mathrm{f}}^+ = \Delta_{\mathrm{s}\to\mathrm{f}}\left(x_{\mathrm{s}}^-, u^-\right), & \left(x_{\mathrm{s}}^-, u^-\right) \in S_{\mathrm{s}\to\mathrm{f}} \end{cases} \tag{48}$$

$$\Sigma_{\mathrm{f}} : \begin{cases} \dot{x}_{\mathrm{f}} = f_{\mathrm{f}}\left(x_{\mathrm{f}}\right) + g_{\mathrm{f}}\left(x_{\mathrm{f}}\right) u, & x_{\mathrm{f}}^- \notin S_{\mathrm{f}\to\mathrm{s}} \\ x_{\mathrm{s}}^+ = \Delta_{\mathrm{f}\to\mathrm{s}}\left(x_{\mathrm{f}}^-\right), & x_{\mathrm{f}}^- \in S_{\mathrm{f}\to\mathrm{s}} \end{cases}$$

III. CONTROL DESIGN FOR RUNNING

This section presents a controller for inducing stable running motions on MABEL. The controller will create an actuated compliant HZD, and enable active force control within the HZD.

Similar to walking, a set of virtual constraints is chosen so that the open-loop compliance of the system is preserved as a dominant characteristic of the closed-loop system. In addition, active force control will be introduced as a means of varying the effective compliance of the system. The motivation for this control approach is elaborated in Section III-A.

This section is organized as follows. Section III-A motivates the control design for embedding active force control within the compliant HZD framework. Section III-B will present a high-level overview of the control design. Section III-C presents the virtual constraints for the stance phase of running that result in a restricted dynamics that is compliant and actuated; the associated zero dynamics are given in Section III-D. Section III-E specifies the controller used for the active force control which provides a means of varying the effective compliance of the system. Section III-F presents the virtual constraints for the flight phase of running and

Section III-G presents the associated zero dynamics. Section III-H presents the hybrid restricted dynamics model. Section III-I presents the optimization process for gait design. Section III-J presents one fixed point representing a periodic running motion. Section III-K presents the closed-loop control design for exponentially stabilizing the periodic orbit.

A. *Motivation for Control Design*

In the walking experiments reported in (Sreenath et al., 2011), the spring on the stance leg compresses on impact and decompresses nearly to its rest position within 100 ms. This property is dependent on the mass of the robot and spring stiffness. Using the same set of springs for running, and with the control strategy of holding the motor position constant at impact, would yield stance times of around 100 ms. Since there is no control authority on the torso in the flight phase due to the conservation of angular momentum, any errors on the torso positions have to be corrected during the stance time. Feedback to correct the potentially large errors for the torso within 100 ms would place large torque requirements on the actuators and would potentially be infeasible.

Hence, longer stance times are necessary. One solution to obtain longer stance times would be to reduce the spring stiffness by physically replacing the springs present in MABEL with softer springs. However, as investigated in Rummel and Seyfarth (Rummel and Seyfarth, 2008), having compliance in the joint level with segmented legs results in a nonlinear relationship between leg compression and leg force. Thus, reducing the spring stiffness on MABEL would have the effect of the robot collapsing at moderate leg compressions owing to the fact that the less stiff spring is not able to provide sufficient leg force to hold up the robot. This would significantly reduce the range of impact angles for the knee for which the springs could support the weight of the robot. Thus, there is a need to vary the effective compliance of the leg in different parts of the stance phase without resorting to softer springs.

We look now at inspiration from biomechanical studies. Ferris et al., (Ferris and Farley, 1997; Ferris et al., 1998) carried out experiments on human runners and found that runners adjust their leg stiffness to accommodate for variations in surface stiffness, allowing them to maintain similar running mechanics (e.g., peak ground reaction force and ground contact time) on different surfaces. Moreover, they suggest that incorporating an adjustable leg stiffness in the design of running robots is important if they are to match the agility and speed of animals on varied terrain. Further, in a set of impressive experiments carried out by Daley et al., (Daley et al., 2006; Daley and Biewener, 2006), where guinea fowl are subjected to large unexpected variations in ground terrain, it is suggested that the animals can accommodate this variation in ground height by varying their leg stiffness.

In summary, there is a need for a control strategy which can dynamically vary the effective compliance of the leg. In addition, active force control has been suggested as a way to increase robustness to perturbations in ground height and ground stiffness in (Koepl et al., 2010). In the following sections, we develop a controller based on virtual constraints and the framework of hybrid zero dynamics to have the capability of dynamically varying the effective leg stiffness.

B. *Overview of the Control Method*

The control objective is to design a periodic running gait that is exponentially stable and sufficiently robust to perturbations so as to accommodate inevitable differences between the model and the robot. Virtual constraints are used to impose constraints on the robot's dynamics in the stance and flight phases. By a judicious choice of variables on which the constraints are to be imposed, the resulting restricted stance dynamics is made compliant and actuated. The control input in the zero dynamics for the stance phase is used to change the effective compliance of the robot. Discrete-event-based control is then employed to (a) create hybrid invariance, (b) exponentially stabilize the periodic gait, and (c) increase the robustness to perturbations in the knee angle at impact and to imperfections in the ground contact model, as will be seen in Section IV

To achieve the control objectives, the feedback controller introduces control on three levels. Figure 6 depicts the overall structure of the running controller. On the first level, continuous-time feedback controllers Γ_p^α with $p \in \mathcal{P} := \{\mathrm{s}, \mathrm{f}\}$ are employed in the stance and flight phases to create invariant and attractive surfaces embedded in the state space for each of the respective phases. The discrete-time feedback controllers $\Gamma_p^{\alpha_c}$ are employed in the transitions between the phases in order to render these surfaces hybrid invariant. For later reference, these surfaces are $\mathcal{Z}_{(\alpha_p, \alpha_c^p, \beta, \gamma)} \subset TQ_p$.

On the second level, an event-based controller Γ^β performs step-to-step parameter updates to render the periodic orbit, representing running and embedded in these surfaces, exponentially stable. Finally, as will be discussed in Section IV, on the third level, another event-based controller Γ^γ performs step-to-step parameter updates to increase the robustness to perturbations in the knee angle at impact and to imperfections in the ground contact model

The remaining sections of this section will develop the procedure described above in greater detail and make it mathematically precise.

C. *Virtual Constraint Design for Stance*

Recall that virtual constraints are holonomic constraints on the robot's configuration variables that are asymptotically imposed through feedback control. They were used in (Sreenath et al., 2011) to synchronize the evolution of the robot's links for synthesizing walking

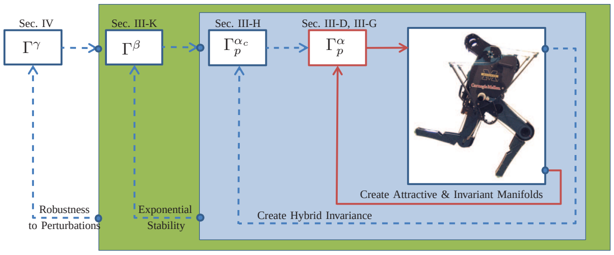

Fig. 6. Feedback diagram illustrating the running controller structure. Continuous lines represent signals in continuous time; dashed lines represent signals in discrete time. The controllers Γ_p^{α} and $\Gamma_p^{\alpha_c}$ create a compliant actuated hybrid zero dynamics. The controller Γ^{β} ensures that the periodic orbit on the resulting zero dynamics manifold is locally exponentially stable. The controller Γ^{γ} increases the robustness to perturbations in the knee angle at impact and to imperfections in the ground contact model.

gaits on MABEL. For walking, one virtual constraint was designed per independent actuator.

For the stance phase of running, the virtual constraints are parametrized by θ_{s}, a strictly monotonic function of the joint configuration variables. As in walking, we choose θ_{s} to be the absolute angle formed by the virtual compliant leg relative to the ground (see Figure 2(a)), i.e.,

$$\theta_{\mathrm{s}}\left(q_{\mathrm{s}}\right) = \pi - q_{\mathrm{LA}_{\mathrm{st}}} - q_{\mathrm{Tor}}. \tag{49}$$

The virtual constraints for the stance phase can then be expressed in the form

$$y_{\mathrm{s}} = h_{\mathrm{s}}\left(q_{\mathrm{s}}\right) = H_0^{\mathrm{s}} q_{\mathrm{s}} - h_d^{\mathrm{s}}\left(\theta_{\mathrm{s}}\right). \tag{50}$$

We have two design choices to make: (a) The controlled variables $H_0^{\mathrm{s}} q_{\mathrm{s}}$, and (b) the constraints $h_d^{\mathrm{s}}\left(\theta_{\mathrm{s}}\right)$.

1) Deciding What to Control: As motivated in the previous section, we need some means of varying the effective compliance of the system for designing running gaits that are robust and have stance phases that are sufficiently long for torso correction to be feasible. Since the transmission of MABEL places a spring in series with the leg shape actuator for the stance leg, $u_{\mathrm{mLS}_{\mathrm{st}}}$, force control on this actuator can be employed to vary the effective compliance of the system. To achieve this, we choose to impose virtual constraints on three controlled variables using three of the actuators and leave the stance motor leg shape actuator for active force control instead of using it for imposing an additional virtual constraint. This increases the dimension of the zero dynamics, which may seem counter-intuitive. Such a strategy of choosing not to implement a virtual constraint using an actuator was employed in the past by Choi and Grizzle (Choi and Grizzle, 2005) for the control of fully actuated planar bipeds with feet by not imposing a virtual constraint using the ankle actuator, and by Poulakakis and Grizzle (Poulakakis and Grizzle, 2009b) on ASLIP, where the leg force actuator is not used to enforce a virtual constraint, but rather used to achieve a target zero dynamics that is diffeomorphic to the dynamics of a SLIP.

By choosing to impose three virtual constraints, we have three control variables to specify. The torso is selected as one of the controlled variables (as was done for walking). Since the torso represents over 65% of the mass of the robot, the entry conditions for the torso into the flight phase are imperative for running. Due to the conservation of angular momentum, there is minimal control authority on the torso position in the flight phase. The initial conditions at the entry into the flight phase essentially determine the evolution of the torso in the flight phase. Next, on the swing leg, the controlled variables are chosen as in walking. In summary, the controlled variables are

$$H_0^{\mathrm{s}} q_{\mathrm{s}} = \begin{bmatrix} q_{\mathrm{LA}_{\mathrm{sw}}} \\ q_{\mathrm{mLS}_{\mathrm{sw}}} \\ q_{\mathrm{Tor}} \end{bmatrix}. \tag{51}$$

2) Specification of the Constraints: The virtual constraints for the stance phase of running are parametrized by 5th order Bézier polynomials. The desired trajectory of each of the controlled variables is denoted by $h_{\mathrm{LA}_{\mathrm{sw}}}^{d,\mathrm{s}}$, $h_{\mathrm{mLS}_{\mathrm{sw}}}^{d,\mathrm{s}}$, and $h_{\mathrm{Tor}}^{d,\mathrm{s}}$ respectively with corresponding Bézier coefficients $\alpha_{\mathrm{LA}_{\mathrm{sw}}}^{\mathrm{s}}$, $\alpha_{\mathrm{mLS}_{\mathrm{sw}}}^{\mathrm{s}}$, and $\alpha_{\mathrm{Tor}}^{\mathrm{s}}$. The desired trajectories of the virtual constraints are assembled as

$$h_d^{\mathrm{s}}\left(\theta_{\mathrm{s}}, \alpha_{\mathrm{s}}\right) = \begin{bmatrix} h_{\mathrm{LA}_{\mathrm{sw}}}^{d,\mathrm{s}}\left(\theta_{\mathrm{s}}, \alpha_{\mathrm{s}}\right) \\ h_{\mathrm{mLS}_{\mathrm{sw}}}^{d,\mathrm{s}}\left(\theta_{\mathrm{s}}, \alpha_{\mathrm{s}}\right) \\ h_{\mathrm{Tor}}^{d,\mathrm{s}}\left(\theta_{\mathrm{s}}, \alpha_{\mathrm{s}}\right) \end{bmatrix}, \tag{52}$$

where the Bézier coefficients are organized as

$$\alpha_{\mathrm{s}} = \begin{bmatrix} \alpha_{\mathrm{LA}_{\mathrm{sw}}}^{\mathrm{s}} \\ \alpha_{\mathrm{mLS}_{\mathrm{sw}}}^{\mathrm{s}} \\ \alpha_{\mathrm{Tor}}^{\mathrm{s}} \end{bmatrix}. \tag{53}$$

Next we discuss the choice of the general shape of the virtual constraints. For running, we expect the torso to be leaning forward during most of the gait. However, a forward torso velocity at the start of flight would result in the torso having an excessive forward pitch at the end of flight due to the conservation of angular momentum, requiring correction of a large torso error during the relatively small (compared to walking) stance phase. To prevent this, the virtual constraint for the torso is designed such that, at the end of the stance phase, the torso is leaning forward but has a backward velocity.

The swing leg virtual constraints are chosen such that the swing leg angle moves forward in the stance phase, and the swing motor leg shape lifts the leg higher to provide ground clearance of the swing leg. These constraints are similar to those designed for walking.

D. Stance Zero Dynamics

The open-loop stance-phase dynamics are given by (14). By a change of coordinates, the inputs to the system can be separated into two pairs - the stance motor leg shape input $u_{\mathrm{mLS}_{\mathrm{st}}}$ with input matrix $B_{\mathrm{mLS}_{\mathrm{st}}}$ and $\tilde{u}$ representing the inputs excluding the stance motor leg shape input, with corresponding input matrix $\tilde{B}$.

With this, the open-loop dynamics can be written in the standard form as,

$$D_{\mathrm{s}}(q_{\mathrm{s}})\,\ddot{q}_{\mathrm{s}} + H_{\mathrm{s}}(q_{\mathrm{s}}, \dot{q}_{\mathrm{s}}) = B_{\mathrm{mLS_{st}}} u_{\mathrm{mLS_{st}}} + \tilde{B}\tilde{u}, \quad (54)$$

where H_s is as in (14). By the choice of the virtual constraints, specifically choosing only three control variables on which the constraints are imposed, the stance motor leg shape input remains free and is not used for imposing a virtual constraint. We intend to implement active force control on the stance motor leg shape input, in which case, this becomes a function of the state, and with an abuse of notation we can write $u_{\mathrm{mLS_{st}}} = u_{\mathrm{mLS_{st}}}(x_{\mathrm{s}})$. With this, the state space representation of the stance dynamics with active force control on the stance motor leg shape input is

$$\begin{aligned}\dot{x}_{\mathrm{s}} &= \begin{bmatrix} \dot{q}_{\mathrm{s}} \\ -D_{\mathrm{s}}^{-1} H_{\mathrm{s}} + D_{\mathrm{s}}^{-1} B_{\mathrm{mLS_{st}}} u_{\mathrm{mLS_{st}}} \end{bmatrix} + \begin{bmatrix} 0 \\ D_{\mathrm{s}}^{-1}\tilde{B} \end{bmatrix} \tilde{u} \\ &=: \tilde{f}_{\mathrm{s}}(x_{\mathrm{s}}) + \tilde{g}_{\mathrm{s}}(x_{\mathrm{s}})\,\tilde{u}. \end{aligned} \quad (55)$$

As discussed in Section III-C, an output function y_{s} has been associated with the continuous stance dynamics with active force control in (55). The zero dynamics is defined as the maximal internal dynamics of the system that is compatible with the output being identically zero (Isidori, 1995). Differentiating the output twice with respect to time results in

$$\frac{d^2 y_{\mathrm{s}}}{dt^2} = L^2_{\tilde{f}_{\mathrm{s}}} h_{\mathrm{s}}(x_{\mathrm{s}}, \alpha_{\mathrm{s}}) + L_{\tilde{g}_{\mathrm{s}}} L_{\tilde{f}_{\mathrm{s}}} h_{\mathrm{s}}(q_{\mathrm{s}}, \alpha_{\mathrm{s}})\,\tilde{u}, \quad (56)$$

where $L_{\tilde{g}_{\mathrm{s}}} L_{\tilde{f}_{\mathrm{s}}} h_{\mathrm{s}}(q_{\mathrm{s}}, \alpha_{\mathrm{s}})$, the decoupling matrix, has full rank. Under the conditions of (Westervelt et al., 2007, Lemma 5.1),

$$u^*_{\mathrm{s}}(x_{\mathrm{s}}, \alpha_{\mathrm{s}}) := -\left(L_{\tilde{g}_{\mathrm{s}}} L_{\tilde{f}_{\mathrm{s}}} h_{\mathrm{s}}(q_{\mathrm{s}}, \alpha_{\mathrm{s}})\right)^{-1} L^2_{\tilde{f}_{\mathrm{s}}} h_{\mathrm{s}}(x_{\mathrm{s}}, \alpha_{\mathrm{s}}), \quad (57)$$

is the unique control input that renders the smooth six-dimensional embedded submanifold

$$\mathcal{Z}_{\alpha_{\mathrm{s}}} = \left\{ x_{\mathrm{s}} \in TQ_{\mathrm{s}} \mid h_{\mathrm{s}}(q_{\mathrm{s}}, \alpha_{\mathrm{s}}) = 0, L_{\tilde{f}_{\mathrm{s}}} h_{\mathrm{s}}(x_{\mathrm{s}}, \alpha_{\mathrm{s}}) = 0 \right\} \quad (58)$$

invariant under the stance dynamics (55); that is, for every $z_{\mathrm{s}} \in \mathcal{Z}_{\alpha_{\mathrm{s}}}$,

$$f^*_{\mathrm{s}}(z_{\mathrm{s}}) := \tilde{f}_{\mathrm{s}}(z_{\mathrm{s}}) + \tilde{g}_{\mathrm{s}}(z_{\mathrm{s}})\, u^*_{\mathrm{s}} \in T_{z_{\mathrm{s}}} \mathcal{Z}_{\alpha_{\mathrm{s}}}. \quad (59)$$

Achieving the virtual constraints by zeroing the corresponding outputs reduces the dimension of the system by restricting its dynamics to the submanifold $\mathcal{Z}_{\alpha_{\mathrm{s}}}$ embedded in the continuous-time state space TQ_{s}. $\mathcal{Z}_{\alpha_{\mathrm{s}}}$ is called the zero dynamics manifold and the restriction dynamics $\dot{z}_{\mathrm{s}} = f^*_{\mathrm{s}}|_{\mathcal{Z}_{\alpha_{\mathrm{s}}}}(z)$ is called the zero dynamics. As we will see next, the zero dynamics is actuated.

As was done in walking, from the Lagrangian dynamics, a valid set of coordinates on $\mathcal{Z}_{\alpha_{\mathrm{s}}}$ is

$$x^{\mathrm{s}}_{zd} = \begin{bmatrix} \xi^{\mathrm{s}}_1 \\ \xi^{\mathrm{s}}_2 \\ \xi^{\mathrm{s}}_3 \\ \xi^{\mathrm{s}}_4 \\ \xi^{\mathrm{s}}_5 \\ \xi^{\mathrm{s}}_6 \end{bmatrix} = \begin{bmatrix} \theta_{\mathrm{s}} \\ q_{\mathrm{Bsp_{st}}} \\ q_{\mathrm{mLS_{st}}} \\ \frac{\partial \mathcal{L}_{\mathrm{s}}}{\partial \dot{q}_{\mathrm{Bsp_{st}}}} \\ \frac{\partial \mathcal{L}_{\mathrm{s}}}{\partial \dot{q}_{\mathrm{mLS_{st}}}} \\ \frac{\partial \mathcal{L}_{\mathrm{s}}}{\partial \dot{q}_{\mathrm{Tor}}} \end{bmatrix}. \quad (60)$$

This set of coordinates explicitly contains the $\mathrm{B_{spring}}$ variable, which illustrates clearly that the zero dynamics is compliant:

$$\dot{x}^{\mathrm{s}}_{zd} = \begin{bmatrix} \dot{\xi}^{\mathrm{s}}_1 \\ \dot{\xi}^{\mathrm{s}}_2 \\ \dot{\xi}^{\mathrm{s}}_3 \\ \dot{\xi}^{\mathrm{s}}_4 \\ \dot{\xi}^{\mathrm{s}}_5 \\ \dot{\xi}^{\mathrm{s}}_6 \end{bmatrix} = \begin{bmatrix} \mathcal{L}_{\tilde{f}_{\mathrm{s}}} \theta_{\mathrm{s}} \\ \mathcal{L}_{\tilde{f}_{\mathrm{s}}} q_{\mathrm{Bsp_{st}}} \\ \mathcal{L}_{\tilde{f}_{\mathrm{s}}} q_{\mathrm{mLS_{st}}} \\ \frac{\partial \mathcal{L}_{\mathrm{s}}}{\partial q_{\mathrm{Bsp_{st}}}} + \tau_{sp} \\ \frac{\partial \mathcal{L}_{\mathrm{s}}}{\partial q_{\mathrm{mLS_{st}}}} \\ \frac{\partial \mathcal{L}_{\mathrm{s}}}{\partial q_{\mathrm{Tor}}} \end{bmatrix} + \begin{bmatrix} 0 \\ 0 \\ 0 \\ 0 \\ u_{\mathrm{mLS_{st}}} \\ 0 \end{bmatrix}. \quad (61)$$

Since the stance motor leg shape input explicitly appears in the zero dynamics, in addition to being compliant, the zero dynamics for the stance phase is also actuated. The force control we intend to implement needs to be a function of the state on the zero dynamics, i.e., $u_{\mathrm{mLS_{st}}} = u_{\mathrm{mLS_{st}}}(z_{\mathrm{s}})$.

E. Active Force Control - Virtual Compliance

Through the choice of the virtual constraints, specifically choosing only three control variables on which the constraints are imposed, the stance motor leg shape input was left free and not used for imposing a virtual constraint. Thus we have a choice of the feedback control to impose on this input. Among all the different feedbacks that one can implement, we choose something very simple - create a virtual compliant element. By defining the feedback,

$$u_{\mathrm{mLS_{st}}}(x_{\mathrm{s}}) = -k_{\mathrm{vc}}\left(q_{\mathrm{mLS_{st}}} - q_{\mathrm{mLS_{vc}}}\right), \quad (62)$$

a virtual compliant element of stiffness k_{vc}, and rest position $q_{\mathrm{mLS_{vc}}}$ is implemented using the motor leg shape actuator. An additional damping element could be added if desired. The transmission of MABEL places this virtual compliant element in series with the physical compliance. Since both these compliances are in series, this method provides a means of dynamically varying the effective compliance of the system.

This method of creating a virtual compliant element using the choice of virtual constraints developed here has already shown great experimental promise and was instrumental in maintaining good ground contact forces for large step-down experiments (see (Park et al., 2011) for 5 inches step-down, and (Park et al., 2012) for up to 8 inches step-down.) As will be seen in Section IV-C, virtual compliance can easily account for cable stretch that was not part of the model for the control design. Further, as suggested in (Rummel and Seyfarth, 2008), depending on the knee angle at impact, the spring force appearing at the stance knee has a nonlinear relation to the spring compression, effectively making the spring softer as the knee bends. Using virtual compliance, one can vary the effective compliance based on the knee angle at impact to account for this phenomenon, thereby preventing the stance knee from excessively bending. Virtual compliance can also be used to easily account for asymmetry in the robot. Further, there is a reduction in the number of parameters to be found in the optimization problem which will be discussed in Section III-I. Finally, another potential benefit would be to use this method for rapid motions, where moving a joint from one position to another as fast as possible is sought rather than accurately moving it along a desired trajectory between two points as typically done in virtual constraints.

One potential disadvantage would be that we are trying to implement compliance using an actuator. On its own, this has several problems associated with high bandwidth requirements on the actuator, and bad efficiency since the actuator would be required to do negative work. However, in this case, since the virtual compliance is in series with a physical compliance, the real spring would handle the high bandwidth and potentially perform any negative work. In which case, this is not a severe disadvantage of the proposed method. Further analysis, beyond the scope of the current work, should be done to confirm this.

For future use, we assemble the independent parameters of the virtual compliance as $\alpha_{\mathrm{vc}} \in \mathbb{R}^2$ and defined as

$$\alpha_{\mathrm{vc}} = \begin{bmatrix} k_{\mathrm{vc}} \\ q_{\mathrm{mLS_{vc}}} \end{bmatrix}. \tag{63}$$

F. Virtual Constraint Design for Flight

During the flight phase, neither foot is in contact with the ground. The stance leg refers to the leg that was the stance leg in the previous stance phase, and similarly for the swing leg. For the flight phase, we have four actuators available to impose virtual constraints. One virtual constraint is designed per independent actuator.

The virtual constraints in the flight phase are parametrized by θ_{f}, a strictly monotonic function of the joint configuration variables. For running, we choose θ_{f} to be the horizontal position of the hip[1], i.e.,

$$\theta_{\mathrm{f}}\left(q_{\mathrm{f}}\right) = p^h_{\mathrm{hip}}. \tag{64}$$

The virtual constraints for the flight phase can then be expressed in the form

$$y_{\mathrm{f}} = h_{\mathrm{f}}\left(q_{\mathrm{f}}\right) = H^{\mathrm{f}}_0 q_{\mathrm{f}} - h^{\mathrm{f}}_d\left(\theta_{\mathrm{f}}\right). \tag{65}$$

Next we have a choice of which variables we choose to be the control variables on which the virtual constraints are imposed. For the flight phase, on the stance leg, the leg angle and the motor leg shape are chosen. The stance foot needs to be lifted off the ground rapidly and this can be achieved by bending the leg by repositioning the stance motor leg shape, and also by moving the leg backward by repositioning the stance leg angle. On the swing leg, the swing foot needs to be unfolded in preparation for an impact. This can be achieved by repositioning the swing motor leg shape. Finally, for directly specifying the touchdown angle, the absolute leg angle of the swing leg is taken as a control variable. This has an added advantage that if the torso pitches forward excessively, the swing leg angle automatically repositions such that the absolute leg angle is the desired value at touchdown. In summary, the controlled variables are

$$H^{\mathrm{f}}_0 q_{\mathrm{f}} = \begin{bmatrix} q_{\mathrm{mLS_{st}}} \\ q_{\mathrm{LA_{sw}}} + q_{\mathrm{Tor}} \\ q_{\mathrm{mLS_{sw}}} \\ q_{\mathrm{LA_{st}}} \end{bmatrix}. \tag{66}$$

The virtual constraints are parametrized by 5th order Bézier polynomials. The desired evolution of each of the controlled variables are denoted by $h^{d,\mathrm{f}}_{\mathrm{mLS_{st}}}$, $h^{d,\mathrm{f}}_{\mathrm{LA}_{abssw}}$, $h^{d,\mathrm{f}}_{\mathrm{mLS_{sw}}}$, and $h^{d,\mathrm{f}}_{\mathrm{LA_{st}}}$ respectively with corresponding Bézier coefficients $\alpha^{\mathrm{f}}_{\mathrm{mLS_{st}}}$, $\alpha^{\mathrm{f}}_{\mathrm{LA}_{abssw}}$, $\alpha^{\mathrm{f}}_{\mathrm{mLS_{sw}}}$, and $\alpha^{\mathrm{f}}_{\mathrm{LA_{st}}}$. The desired evolution of the virtual constraints are assembled as

$$h^{\mathrm{f}}_d\left(\theta_{\mathrm{f}}, \alpha_{\mathrm{f}}\right) = \begin{bmatrix} h^{d,\mathrm{f}}_{\mathrm{mLS_{st}}}\left(\theta_{\mathrm{f}}, \alpha_{\mathrm{f}}\right) \\ h^{d,\mathrm{f}}_{\mathrm{LA}_{abssw}}\left(\theta_{\mathrm{f}}, \alpha_{\mathrm{f}}\right) \\ h^{d,\mathrm{f}}_{\mathrm{mLS_{sw}}}\left(\theta_{\mathrm{f}}, \alpha_{\mathrm{f}}\right) \\ h^{d,\mathrm{f}}_{\mathrm{LA_{st}}}\left(\theta_{\mathrm{f}}, \alpha_{\mathrm{f}}\right) \end{bmatrix}, \tag{67}$$

where the Bézier coefficients are organized as

$$\alpha_{\mathrm{f}} = \begin{bmatrix} \alpha^{\mathrm{f}}_{\mathrm{mLS_{st}}} \\ \alpha^{\mathrm{f}}_{\mathrm{LA}_{abssw}} \\ \alpha^{\mathrm{f}}_{\mathrm{mLS_{sw}}} \\ \alpha^{\mathrm{f}}_{\mathrm{LA_{st}}} \end{bmatrix}. \tag{68}$$

G. Flight Zero Dynamics

The flight zero dynamics is relatively straightforward since all actuators are employed to enforce virtual constraints. The output function y_{f} is associated with the continuous flight dynamics defined in (21). Differentiating the output twice with respect to time results in

$$\frac{d^2 y_{\mathrm{f}}}{dt^2} = L^2_{f_{\mathrm{f}}} h_{\mathrm{f}}\left(x_{\mathrm{f}}, \alpha_{\mathrm{f}}\right) + L_{g_{\mathrm{f}}} L_{f_{\mathrm{f}}} h_{\mathrm{f}}\left(q_{\mathrm{f}}, \alpha_{\mathrm{f}}\right) u, \tag{69}$$

where $L_{g_{\mathrm{f}}} L_{f_{\mathrm{f}}} h_{\mathrm{f}}\left(q_{\mathrm{f}}, \alpha_{\mathrm{f}}\right)$, the decoupling matrix, has full rank. Under the conditions of (Westervelt et al., 2007, Lemma 5.1),

$$u^*_{\mathrm{f}}\left(x_{\mathrm{f}}, \alpha_{\mathrm{f}}\right) := -\left(L_{g_{\mathrm{f}}} L_{f_{\mathrm{f}}} h_{\mathrm{f}}\left(q_{\mathrm{f}}, \alpha_{\mathrm{f}}\right)\right)^{-1} L^2_{f_{\mathrm{f}}} h_{\mathrm{f}}\left(x_{\mathrm{f}}, \alpha_{\mathrm{f}}\right), \tag{70}$$

---

[1] Ideally, the horizontal position of the COM would be a good choice, since it is guaranteed to be strictly monotonic in the flight phase. However, for experimental convenience, and due the fact that the torso for MABEL is heavy and the legs relatively light weight, the horizontal position of the hip would also be monotonic.

is the unique control input that renders the smooth six-dimensional embedded submanifold

$$\mathcal{Z}_{\alpha_{\mathrm{f}}} = \{x_{\mathrm{f}} \in TQ_{\mathrm{f}} \mid h_{\mathrm{f}}\left(q_{\mathrm{f}}, \alpha_{\mathrm{f}}\right) = 0, L_{f_{\mathrm{f}}} h_{\mathrm{f}}\left(x_{\mathrm{f}}, \alpha_{\mathrm{f}}\right) = 0\} \tag{71}$$

invariant under the flight dynamics (21); that is, for every $z_{\mathrm{f}} \in \mathcal{Z}_{\alpha_{\mathrm{f}}}$,

$$f_{\mathrm{f}}^{*}\left(z_{\mathrm{f}}\right) := f_{\mathrm{f}}\left(z_{\mathrm{f}}\right) + g_{\mathrm{f}}\left(z_{\mathrm{f}}\right) u_{\mathrm{f}}^{*} \in T_{z_{\mathrm{f}}} \mathcal{Z}_{\alpha_{\mathrm{f}}}. \tag{72}$$

Achieving the virtual constraints by zeroing the corresponding outputs reduces the dimension of the system by restricting its dynamics to the submanifold $\mathcal{Z}_{\alpha_{\mathrm{f}}}$ embedded in the continuous-time state space TQ_{f}. $\mathcal{Z}_{\alpha_{\mathrm{f}}}$ is called the zero dynamics manifold and the restriction dynamics $\dot{z}_{\mathrm{f}} = f_{\mathrm{f}}^{*}|_{\mathcal{Z}_{\alpha_{\mathrm{f}}}}\left(z_{\mathrm{f}}\right)$ is called the zero dynamics.

From Lagrangian dynamics, a valid set of coordinates on $\mathcal{Z}_{\alpha_{\mathrm{f}}}$ is

$$x_{zd}^{\mathrm{f}} = \begin{bmatrix} \xi_1^{\mathrm{f}} \\ \xi_2^{\mathrm{f}} \\ \xi_3^{\mathrm{f}} \\ \xi_4^{\mathrm{f}} \\ \xi_5^{\mathrm{f}} \\ \xi_6^{\mathrm{f}} \end{bmatrix} = \begin{bmatrix} q_{\mathrm{Tor}} \\ p_{\mathrm{hip}}^{h} \\ p_{\mathrm{hip}}^{v} \\ \frac{\partial \mathcal{L}_{\mathrm{f}}}{\partial \dot{q}_{\mathrm{Tor}}} \\ \frac{\partial \mathcal{L}_{\mathrm{f}}}{\partial \dot{p}_{\mathrm{hip}}^{h}} \\ \frac{\partial \mathcal{L}_{\mathrm{f}}}{\partial \dot{p}_{\mathrm{hip}}^{v}} \end{bmatrix}. \tag{73}$$

These coordinates are different from those chosen for RABBIT in (Westervelt et al., 2007, Chap. 9). Since the flight dynamics for MABEL, developed in Section II-B2, incorporates the boom dynamics, the angular momentum is not strictly conserved and a different set of coordinates for the zero dynamics is required. The zero dynamics is then given by

$$\dot{x}_{zd}^{\mathrm{f}} = \begin{bmatrix} \dot{\xi}_1^{\mathrm{f}} \\ \dot{\xi}_2^{\mathrm{f}} \\ \dot{\xi}_3^{\mathrm{f}} \\ \dot{\xi}_4^{\mathrm{f}} \\ \dot{\xi}_5^{\mathrm{f}} \\ \dot{\xi}_6^{\mathrm{f}} \end{bmatrix} = \begin{bmatrix} L_{f_{\mathrm{f}}} q_{\mathrm{Tor}} \\ L_{f_{\mathrm{f}}} p_{\mathrm{hip}}^{h} \\ L_{f_{\mathrm{f}}} p_{\mathrm{hip}}^{v} \\ \frac{\partial \mathcal{L}_{\mathrm{f}}}{\partial q_{\mathrm{Tor}}} \\ \frac{\partial \mathcal{L}_{\mathrm{f}}}{\partial p_{\mathrm{hip}}^{h}} \\ \frac{\partial \mathcal{L}_{\mathrm{f}}}{\partial p_{\mathrm{hip}}^{v}} \end{bmatrix}. \tag{74}$$

H. Event Transitions

The division of running into the stance and flight phases necessitates the specification of transition maps between the phases. In preparation for the next section, we introduce correction polynomials so as to obtain hybrid invariance of the zero dynamics manifolds. We also model the hybrid dynamics on the zero dynamics manifold by concatenating the solutions of the parameter dependent hybrid systems for each subphase.

On transition from stance to flight or flight to stance, we require the post-transition solution to be on the zero dynamics of the subsequent phase. This ensures the zero dynamics manifold is hybrid invariant and enables us to study the behavior of the restricted hybrid system. Hybrid invariance is achieved by introducing correction polynomials (Morris and Grizzle, 2009; Grizzle et al., 2008) which are parametrized by Bézier coefficients and are updated at event transitions such that the post-transition state lies in the zero dynamics manifold of the next phase. This is obtained by modifying the virtual constraint at event transitions by introducing new outputs for each of the the phases $p \in \mathcal{P}$

$$\begin{aligned} y_c^p &= h_p\left(q_p, \alpha_p, \alpha_c^p\right) \\ &= H_0^p q_p - h_d^p\left(\theta_p, \alpha_p\right) - h_c^p\left(\theta_p, \alpha_p^c\right). \end{aligned} \tag{75}$$

The output consists of the previous output (50), (65), and an additional correction term h_c^p such that the post transition output and its velocity are zero, i.e., $y_c^{p+} = 0, \dot{y}_c^{p+} = 0$. This is achieved by choosing the Bézier coefficients α_c^p appropriately. Moreover, the correction polynomial is designed in such a way that the modified virtual constraint is smoothly joined to the original virtual constraint at the middle of the current phase. The zero dynamics defined in Sections III-D, and III-G can be defined to incorporate the new output with correction polynomial to obtain the zero dynamics manifolds $\mathcal{Z}_{\alpha_p, \alpha_c^p}$.

Next, to implement a deadbeat event-based control strategy to modify the virtual compliance parameters during the stance phase of running, the stance phase is broken into two subphases: the stance-compression (sc) and the stance-decompression (sd). The framework of virtual constraints with subphases, as developed for walking (see (Sreenath et al., 2011, App. A),) is used to ensure that the division of the stance phase does not affect the parametrization of virtual constraints presented in Section III-C. The hybrid zero dynamics model for running that captures the continuous-time dynamics of the system in stance-compression subphase, stance-decompression subphase, the flight phase, and the discrete transitions among them, is given by

$$\begin{aligned} &\Sigma_{zd}^{\mathrm{s}} : \left\{ \begin{array}{l} \Sigma_{zd}^{sc} : \left\{ \begin{array}{rl} \left.\begin{array}{r} \dot{z}_{\mathrm{s}} = f_{\mathrm{s}}^{*}\left(z_{\mathrm{s}}\right) \\ \dot{\alpha}_{\mathrm{vc}} = 0 \end{array}\right\} & z_{\mathrm{s}} \notin \mathcal{S}_{sc \to sd} \\ \left.\begin{array}{r} z_{\mathrm{s}}^{sd+} = \Delta_{sc \to sd}\left(z_{\mathrm{s}}^{sc-}\right) \\ \alpha_{\mathrm{vc}}^{sd+} = \alpha_{\mathrm{vc}}^{sd}, \end{array}\right\} & z_{\mathrm{s}} \in \mathcal{S}_{sc \to sd} \end{array} \right. \\ \Sigma_{zd}^{sd} : \left\{ \begin{array}{rl} \left.\begin{array}{r} \dot{z}_{\mathrm{s}} = f_{\mathrm{s}}^{*}\left(z_{\mathrm{s}}\right) \end{array}\right\} & z_{\mathrm{s}} \notin \mathcal{S}_{sd \to \mathrm{f}} \\ \left.\begin{array}{r} \dot{\alpha}_{\mathrm{vc}} = 0 \\ z_{\mathrm{f}}^{+} = \Delta_{sd \to \mathrm{f}}\left(z_{\mathrm{s}}^{sd-}\right) \end{array}\right\} & z_{\mathrm{s}} \in \mathcal{S}_{sd \to \mathrm{f}} \end{array} \right. \end{array} \right. \\ &\Sigma_{zd}^{\mathrm{f}} : \left\{ \begin{array}{rl} \left.\begin{array}{r} \dot{z}_{\mathrm{f}} = f_{\mathrm{f}}^{*}\left(z_{\mathrm{f}}\right) \end{array}\right\} & z_{\mathrm{f}} \notin \mathcal{S}_{\mathrm{f} \to sc} \\ \left.\begin{array}{r} z_{\mathrm{s}}^{+} = \Delta_{\mathrm{f} \to sc}\left(z_{\mathrm{f}}^{-}\right) \\ \alpha_{\mathrm{vc}}^{sc+} = \alpha_{\mathrm{vc}}^{sc} \end{array}\right\} & z_{\mathrm{f}} \in \mathcal{S}_{\mathrm{f} \to sc} \end{array} \right. \end{aligned} \tag{76}$$

where $z_{\mathrm{s}} \in \mathcal{Z}_{\alpha_{\mathrm{s}}, \alpha_c^{\mathrm{s}}}$ and $z_{\mathrm{f}} \in \mathcal{Z}_{\alpha_{\mathrm{f}}, \alpha_c^{\mathrm{f}}}$ are the stance and flight zero dynamics coordinates respectively, $\alpha_{\mathrm{vc}} \in \mathbb{R}^2$ is the virtual compliance parameters, and α_{vc}^{p} for $p \in \mathcal{P}_{\mathrm{s}} := \{sc, sd\}$ are the constant independent parameters for the virtual compliance that are to be specified.

The switching surfaces for the transitions are defined as

$$\begin{aligned} \mathcal{S}_{sc\to sd} &= \left\{ z_{\mathrm{s}} \in \mathcal{Z}_{\alpha_{\mathrm{s}},\alpha_{\mathrm{c}}^{\mathrm{s}}} \mid H_{sc\to sd}\left(z_{\mathrm{s}}\right)=0 \right\} \\ \mathcal{S}_{sd\to \mathrm{f}} &= \left\{ z_{\mathrm{s}} \in \mathcal{Z}_{\alpha_{\mathrm{s}},\alpha_{\mathrm{c}}^{\mathrm{s}}} \mid H_{sd\to \mathrm{f}}\left(z_{\mathrm{s}}\right)=0 \right\} . \\ \mathcal{S}_{\mathrm{f}\to sc} &= \left\{ z_{\mathrm{f}} \in \mathcal{Z}_{\alpha_{\mathrm{f}},\alpha_{\mathrm{c}}^{\mathrm{f}}} \mid H_{\mathrm{f}\to sc}\left(z_{\mathrm{f}}\right)=0 \right\} \end{aligned} \tag{77}$$

The threshold functions given below

$$\begin{aligned} H_{sc\to sd} &:= \theta_{\mathrm{s}} - \theta_{sd} \\ H_{sd\to \mathrm{f}} &:= H_{\mathrm{s}\to \mathrm{f}} \\ H_{\mathrm{f}\to sc} &:= H_{\mathrm{f}\to \mathrm{s}}, \end{aligned} \tag{78}$$

where θ_{sd} is a independent parameter to be specified, $H_{\mathrm{s}\to\mathrm{f}}$ and $H_{\mathrm{f}\to\mathrm{s}}$ are as as defined in Sections II-C1, II-C2 respectively. Note that the stance to flight threshold function is defined as $H_{\mathrm{s}\to\mathrm{f}} : \mathcal{S}_{\mathrm{s}\to\mathrm{f}} \times \mathcal{U} \to \mathbb{R}$. However, with the inputs all being a function of the state (refer (57), (62)), this transition is then essentially defined on the stance to flight switching surface, $\mathcal{S}_{\mathrm{s}\to\mathrm{f}}$. The transition maps provide the initial conditions for the ensuing phase and are given below

$$\begin{aligned} \Delta_{sc\to sd} &:= \mathrm{i}d \\ \Delta_{sd\to \mathrm{f}} &:= \Delta_{\mathrm{s}\to \mathrm{f}} \\ \Delta_{\mathrm{f}\to sc} &:= \Delta_{\mathrm{f}\to \mathrm{s}}, \end{aligned} \tag{79}$$

with $\Delta_{\mathrm{s}\to\mathrm{f}}$, $\Delta_{\mathrm{f}\to\mathrm{s}}$ as defined in Sections II-C1, II-C2 respectively. Note that the stance to flight transition function is defined as $\Delta_{\mathrm{s}\to\mathrm{f}} : TQ_{\mathrm{s}} \times \mathcal{U} \to TQ_{\mathrm{f}}$. However, as mentioned earlier, since the inputs are a function of the state, this mapping is essentially from the stance state space.

To find the set of values for the independent parameters of the constraint design, and parameters of the virtual compliance, we employ the above restricted lower-dimensional hybrid system and formulate the problem as a constrained optimization.

I. Gait Design Through Optimization

A periodic running gait is designed by selecting the free parameters in the virtual constraints, and the virtual compliance. As was carried out for gait design for walking in (Sreenath et al., 2011), an optimization problem is posed to minimize energy per step length, subject to constraints to meet periodicity, workspace and actuator limitations. The equations of the hybrid zero dynamic model developed in the earlier section, which are of reduced dimension compared to the full dynamics, are employed for efficiency of computation.

The cost function is given by,

$$J_{nom}\left(\alpha_{\mathrm{s}}, \alpha_{\mathrm{f}}, \alpha_{\mathrm{vc}}^{sc}, \alpha_{\mathrm{vc}}^{sd}\right) = \frac{1}{p^{h}_{\mathrm{toe_{sw}}}\left(q_{\mathrm{f}}^{-}\right)} \int_{0}^{T_I} ||u(t)||^2 dt, \tag{80}$$

where T_I is the step duration (stance plus flight time) and $p^{h}_{\mathrm{toe_{sw}}}$ is the step length. Minimizing this cost function tends to reduce peak torque demands and minimize the electrical energy consumed per step.

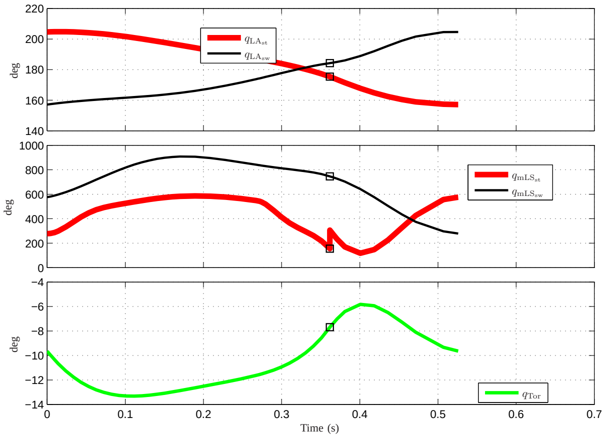

Fig. 7. Evolution of the virtual constraints and configuration variables for a nominal fixed point (periodic running gait) at a speed of 1.34 m/s and step length 0.7055 m. The squares illustrate the location of transition between stance to flight phase.

J. Fixed Point for Running

This section presents a nominal periodic running gait at 1.34 m/s obtained by applying the optimization procedure outlined in Section III-I to the virtual constraints of Sections III-C, III-F, the virtual compliance of Section III-E, and with the cost function (80). Figure 7 illustrates the nominal evolution of the virtual constraints for the stance and flight phases, along with other configuration variables, for one step of running. The squares on the plots indicate the transition from stance to flight phase. The step time is 525 ms with 69% spent in stance and 31% in flight. On entry into the flight phase, the torso is leaning forward (negative torso angle) and is rotating backward (positive torso velocity). The swing leg angle travels roughly 57% of its total $47.5°$ during the stance phase[2] and needs to travel the remaining 43% in the flight phase which is of smaller duration. Thus the velocities of the joints in the flight are high compared to those of the stance phase. The instantaneous change in the stance motor leg shape position on transition to flight is to reset the stance spring to its rest position in the flight phase.

Figure 8 illustrates the evolution of the leg shape and the stance $\mathrm{B_{spring}}$ variables. The squares in the plot indicate the stance to flight transition and the circle in the spring plot indicates the stance-compression to stance-decompression transition. During the flight phase, the stance leg shape initially unfolds due to the large velocity of push-off during the final part of the stance phase as the spring rapidly decompresses. During the stance-compression phase the spring compresses, reaches its peak value of almost $36°$ and starts to decompress. On transition to the stance-decompression phase, the motor injects energy into the system causing the spring to rapidly compress to a peak of $47°$. At lift-off, when the

---

[2] Contrast this to that of humans, where the legs travel rougly 90% of the range of travel during the stance phase.

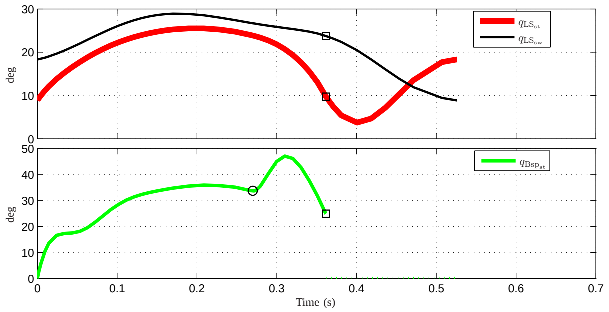

Fig. 8. Evolution of the leg shape and stance $\mathrm{B_{spring}}$ variables corresponding to the nominal fixed point. The squares illustrate the location of transition between stance to flight phase. The circle on the $\mathrm{B_{spring}}$ plot illustrates the location of the *sc* to *sd* event transition.

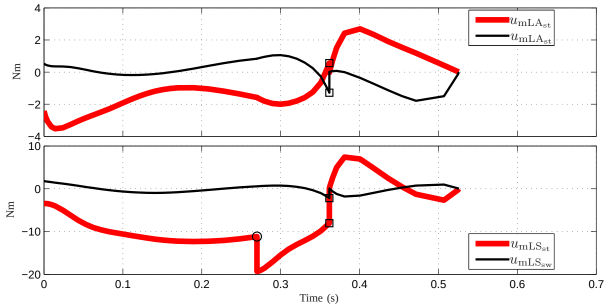

Fig. 9. Actuator torques corresponding to the nominal fixed point. The squares illustrate the location of transition between stance to flight phase. The circle on the $u\mathrm{mLS_{st}}$ plot illustrates the location of the *sc* to *sd* event transition. Note that the torques are discontinuous at stance to flight transitions. Also note the additional discontinuity for $u\mathrm{mLS_{st}}$ at the *sc* to *sd* event transition due to the instantaneous change in the offset for the virtual compliance at this transition.

vertical component of the ground reaction force goes to zero, the spring is compressed to approximately $25°$.

Figure 9 illustrates the actuator torques used to realize the gait. The stance and swing leg angle torques and the swing leg shape torque are small compared to the peak torque capacities of the actuators: 30Nm. The stance leg shape torque is large, initially to support the weight of the robot as the stance knee bends and subsequently to provide a large energy injection in the stance-decompression phase to achieve lift-off. The stance motor leg shape torque is discontinuous at the stance-compression to stance-decompression transition due to an instantaneous change in the parameters for the virtual compliance. All torques are discontinuous on the stance to flight transition due to the impact of the spring with the hard-stop.

Figure 10 illustrates the evolution of the swing leg height and the vertical position of the center of mass of the robot. The swing foot is over 15 cm above the ground at its peak to offer good ground clearance for hard impacts. During the stance phase, the COM undergoes an asymmetric motion with the lowest point of potential energy being around 52% into the stance phase. During the flight phase, the COM has a ballistic trajectory. Both these motions are dominant characteristics of running.

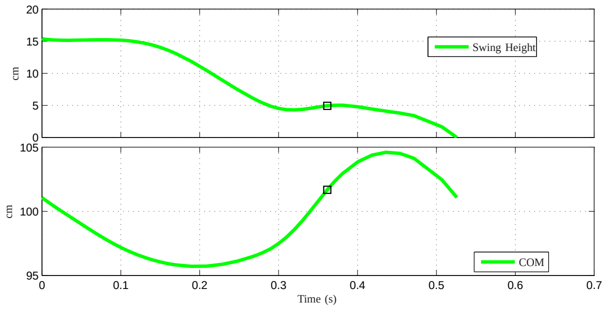

Fig. 10. Evolution of swing leg height and vertical center of mass (COM) of the robot for the nominal fixed point. The COM trajectory clearly illustrates the lowest point of potential energy during the stance phase and the ballistic trajectory in the flight phase, both of which are dominating characteristics of running. The squares illustrate the location of transition between stance to flight phase.

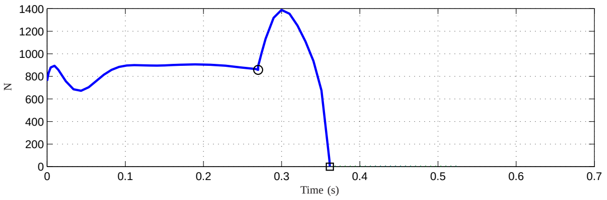

Fig. 11. Vertical component of the ground reaction force for the nominal running fixed point. At the *sc* to *sd* event transition (indicated by the circle), the change in the offset for the virtual compliance causes the spring to compress further which increases the ground reaction force considerably. Takeoff occurs when the ground reaction force goes to zero (indicated by the square.)

Figure 11 illustrates the vertical component of the ground reaction force. Immediately upon impact, during the stance-compression phase, there is a peak in the ground reaction force due to the spring compressing rapidly on impact. During most of the stance-compression phase, the force is fairly constant. On transition to stance-decompression phase, the energy injection causes the force to rapidly first increase and then go to zero at which point stance to flight transition occurs.

K. Closed-loop Design and Stability Analysis

The feedback presented in (57), (62), (70), when used with the modified outputs (75), renders the zero dynamics hybrid invariant. This feedback does not however render the solution stable or attractive in any way. In the following, we introduce control action on two levels with an inner-loop and an outer-loop controller. In Section IV a third level of control action in the form of another outer-loop will be introduced. On the first level, a continuous-time controller is presented that in addition to rendering the zero dynamics invariant also makes it attractive. The hybrid invariance is still achieved through the correction polynomials on a event to event level. On the second level, an outer-loop event-based discrete linear controller is introduced to exponentially stabilize the periodic orbit representing the running gait. As will be seen in Section IV, on the third level, an additional outer-loop event-based discrete nonlinear controller is introduced to increase the robustness to perturbations in the knee angle at impact and to imperfections in the ground contact model.

The classic input-output linearizing controller

$$u = u^*\left(x_p, \alpha_p\right) - L_{g_p} L_{f_p} h_p\left(q_p, \alpha_p\right)^{-1} \left(\frac{K_{p,P}}{\epsilon^2} y_c^p + \frac{K_{p,D}}{\epsilon} \dot{y}_c^p\right), \tag{81}$$

where $p \in \mathcal{P}$, renders the zero dynamics both invariant and attractive. The correction polynomials create hybrid invariance. For ϵ sufficiently small, the stability of the fixed point under this control action can be analyzed through use of the restricted Poincaré map (Morris and Grizzle, 2005), i.e., the Poincaré map associated with the invariant hybrid system presented in Section III-H. We consider $\mathcal{S}_{sc\to sd}$ as a Poincaré section. Then, the stability of the fixed point can be determined by the restricted Poincaré map defined as $\rho : \mathcal{S}_{sc\to sd} \cap \mathcal{Z}_{\alpha_{\mathrm{s}},\alpha_c^{\mathrm{s}}} \to \mathcal{S}_{sc\to sd} \cap \mathcal{Z}_{\alpha_{\mathrm{s}},\alpha_c^{\mathrm{s}}}$. Using this restricted Poincaré map, we can numerically calculate the eigenvalues of its linearization about the fixed point. The analysis shows that the running gait obtained by optimizing (80) and with the closed-loop controller (81) is unstable[3] with a dominant eigenvalue of 1.1928. Thus, an additional controller needs to be designed to stabilize the running fixed point.

Exponentially Stabilizing Outer-loop Controller: An outer-loop discrete event-based linear controller can be designed to stabilize the discrete linear system representing the linearized Poincaré map, as was done for the planar hopper Thumper in (Poulakakis and Grizzle, 2009a) or a 3D biped in (Chevallereau et al., 2009). We identify certain parameters that can be varied step-to-step, and which could possibly affect stability of the fixed point. These are assembled as $\beta \in \mathcal{B}$

$$\beta = \begin{bmatrix} \beta^{sc}_{k_{\mathrm{vc}}} \\ \beta^{sd}_{k_{\mathrm{vc}}} \\ \beta_{TD} \\ \beta^{sc}_{q_{\mathrm{mLS}_{\mathrm{vc}}}} \\ \beta^{sd}_{q_{\mathrm{mLS}_{\mathrm{vc}}}} \\ \beta_{\theta_{\mathrm{f}}} \\ \beta_{\mathrm{Tor}} \end{bmatrix}, \tag{82}$$

where $\beta^p_{k_{\mathrm{vc}}}, \beta^p_{q_{\mathrm{mLS}_{\mathrm{vc}}}}$ are the virtual compliance stiffness and offset for phase p, β_{TD} is the touchdown angle, $\beta_{\theta_{\mathrm{f}}}$ is an offset to be added to θ_{f}^-, and β_{Tor} is the torso offset.

The full-order Poincaré map is considered for the design (and subsequent experimental implementation) of the Γ^β outer-loop event-based controller, and is defined as $P_\beta : \mathcal{S}_\beta \times \mathcal{B} \to \mathcal{S}_\beta$, with $\mathcal{S}_\beta := \mathcal{S}_{sc\to sd}$, such that

$$x_{\mathrm{s}}^{sc-}[k+1] = P_\beta(x_{\mathrm{s}}^{sc-}[k], \beta[k]). \tag{83}$$

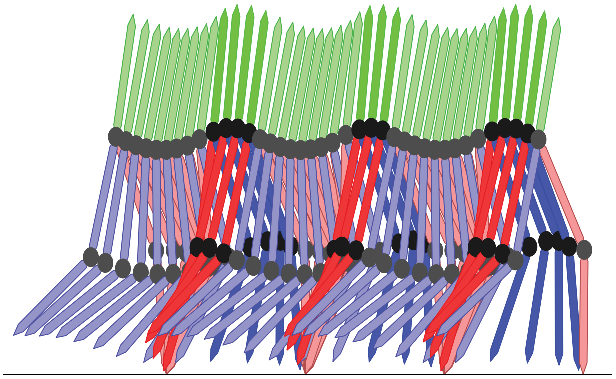

Fig. 12. Stick figure plot of three steps of running. The stance leg is illustrated in red, while the swing leg is illustrated in blue. Stick figures with darker shades are in flight phase, while those with lighter shades are in stance phase. From the stick figure it can be easily deduced that the flight phase lasts around 30% of the gait.

The full-order Poincaré map is linearized about the fixed point to obtain the discrete-time linear system

$$\delta x_{\mathrm{s}}^{sc-}[k+1] = \left.\frac{\partial P_\beta}{\partial x_{\mathrm{s}}^{sc-}}\right|_{(x_{\mathrm{s}}^{sc-*},0)} \delta x_{\mathrm{s}}^{sc-}[k] + \left.\frac{\partial P_\beta}{\partial \beta}\right|_{(x_{\mathrm{s}}^{sc-*},0)} \beta[k], \tag{84}$$

where $\delta x_{\mathrm{s}}^{sc-} = x_{\mathrm{s}}^{sc-} - x_{\mathrm{s}}^{sc-*}$. Discrete LQR is used to design a linear feedback such that the closed-loop eigenvalues are within the unit circle. The feedback can be written as

$$\beta[k] = \Gamma^\beta(\delta x_{\mathrm{s}}^{sc-}[k]) := K_{LQR} \delta x_{\mathrm{s}}^{sc-}[k]. \tag{85}$$

This procedure is carried out numerically, and for the presented fixed point, the dominant eigenvalue of the Poincaré map with the feedback Γ^β is found to be 0.8383, which concludes that the fixed point is locally exponentially stabilized with this controller.

L. Simulations

As seen in the previous section, the obtained running fixed point is unstable, and a static outer-loop event-based controller (Γ^β) was designed through LQR to exponentially stabilize the fixed point. In this section we carry out simulations of the closed-loop system comprised of the open-loop system with the following controllers: Γ_p^α, the continuous-time controller that creates invariant and attractive surfaces embedded in the stance and flight phases, $\Gamma_p^{\alpha_c}$, the discrete-time feedback controller that render these surfaces hybrid invariant, and finally, Γ^β, that performs step-to-step parameter updates to render the periodic orbit exponentially stable.

Figure 12 depicts a stick figure for three steps of the running gait, while Figures 13 - 15 depict phase plots for the first 50 steps of the running simulation, with the position on the x-axis and the velocity on the y-axis.

---

[3] In fact all running fixed points that were found were unstable.

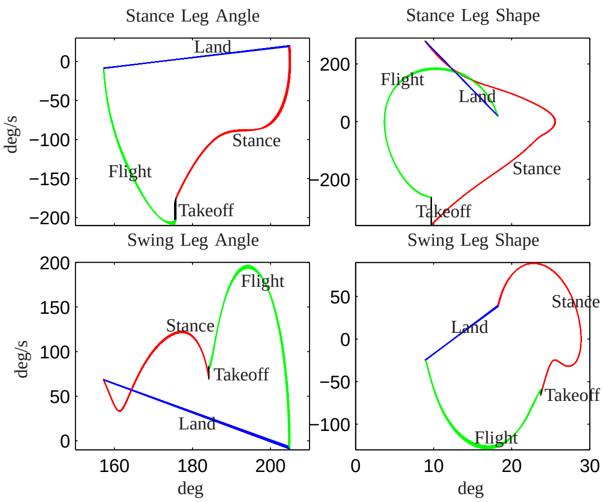

Fig. 13. The four graphs depict the phase plots - joint angles in degrees (x-axis) versus their velocities in degress per second (y-axis) in the following four phases: stance (red), takeoff (black), flight (green) and land (blue). The takeoff phase is the transition from stance to flight with no change in the joint angles and is characterized by vertical trajectories in the phase plot. The land phase is the transition from flight to stance and there is an associated jump in the joint angles due the interchange of the stance and swing limbs on landing. Both these phases model an instantaneous impact.

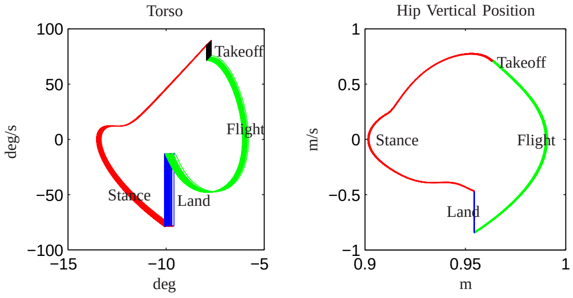

(a) (b)

Fig. 14. Phase plot of (a) torso and (b) vertical position of the hip for the stance (red), takeoff (balck), flight (green) and land (blue) phases. The torso joint angle remains unchanged for both the takeoff and land phases and is characterized by vertical lines in the phase plot. The takeoff phase for the vertical hip position is characterized by a single point on the phase plot indicating no change in position or velocity of the hip on takeoff.

IV. PREPARING FOR EXPERIMENTAL DEPLOYMENT

Next, in preparation for experimental validation, we study the robustness of the controller to perturbations. From the walking experiments, we observe that successful gaits were obtained when the controller could reject perturbations in the form of external forces (Sreenath et al., 2011), ground variations (Park et al., 2011) and structural modifications (see (Grizzle, 2010a)). For running, with the feedback controller comprised of the continuous-time control Γ_p^{α}, the discrete event-based controller $\Gamma_p^{\alpha_c}$ as the inner-loop, and with the discrete event-based controller Γ^{β} as the outer-loop, the robustness to external perturbations is studied. This controller can reject an error in torso of up to 6° in both directions. This is adequate robustness to perturbations in torso angle. However, as shown in Figure 16(a), the controller is unable to reject an error in the form of the stance leg shape at impact ‘being bent by 5° more than the nominal. Thus, there is a need for a controller that can improve the robustness to perturbations in the knee angle at impact. This will be crucial for experimental validation.

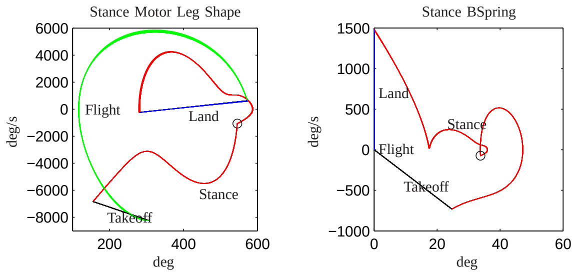

(a) (b)

Fig. 15. Phase plot of (a) stance motor leg shape and (b) stance $B_{\rm spring}$ for the four phases of running: stance (red), takeoff(black), flight (green), and land (blue). Small circles on the plot during the stance phase indicate the location at which the controller switches from stance-compression to stance-decompression subphases. For the stance motor leg shape plot, note that the takeoff phase is not characterized by a horizontal trajectory indicating that on takeoff, there is a change in the angle of the motor leg shape. This is as per the model in Section II-C1. For the stance $B_{\rm spring}$ plot, note that the location of the transition from stance-compression to stance-decompression occurs slightly after peak compression of the spring. The energy injection in the stance-decompression subphase causes the spring to first compress further and then rapidly decompress. The takeoff phase is characterized by a change in the spring position, as per the impact with the hard-stop to keep the position of the linkage variables invariant under this transition. Also for the bspring, the flight phase is a trivial phase and is characterized by a single point on the phase plot. This is due to the model that keeps the spring at its rest position in flight.

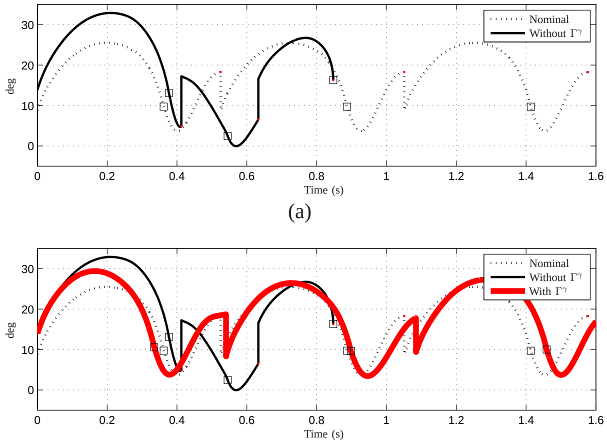

(a)

(b)

Fig. 16. Three step simulation of a 5° perturbation in the impact value of the leg shape. (a) Perturbation without Γ^γ outer-loop controller, (b) Perturbation with Γ^γ outer-loop controller. The nominal (no perturbation) plot is shown for comparision. The squares on the plots indicate locations at which the controller transitions to from stance to flight phase.

A. Nonlinear Outer-loop Controller for Increasing Robustness

The closed-loop system with the continuous-time and discrete-time controllers $\Gamma_\mu^{\alpha}, \Gamma_p^{\alpha_c}$ forming the inner loop to create hybrid invariant and attractive surfaces in the stance and flight state spaces, and the outer-loop controller Γ^{β} exponentially stabilizing the periodic orbit is considered. An additional event-based controller can be designed for this closed-loop hybrid system at an appropriate switching surface. We consider the event corresponding to touchdown, which occurs right after impact with the ground. Designing an event-based controller at this event provides a way to respond to errors arising in the flight phase (such as landing with too much knee bend, or running too fast in the prior step caused by imperfections in the ground contact model, etc.). Mathematically, the switching surface is $\mathcal{S}_{\gamma} := \Delta_{\mathrm{f}\to\mathrm{s}}(\mathcal{S}_{\mathrm{f}\to\mathrm{s}}) \subset TQ_{\mathrm{s}}$. A set of parameters $\gamma \in \mathcal{G}$ is considered and are assembled as

$$\gamma = \begin{bmatrix} \gamma^{sc}_{k_{\mathrm{vc}}} \\ \gamma_{\mathrm{Tor}} \\ \gamma_{\mathrm{LS}_{\mathrm{sw}}} \\ \gamma_{\delta_{sc\to sd}} \end{bmatrix}, \tag{86}$$

where $\gamma^{sc}_{k_{\mathrm{vc}}}$ is the virtual compliance stiffness for the stance-compression subphase, γ_{Tor} is the torso offset, $\gamma_{\mathrm{LS}_{\mathrm{sw}}}$ is an offset that lifts the swing leg higher, $\gamma_{\delta_{sc\to sd}}$ is an offset that shifts the stance-compression to stance-decompression transition event.

A nonlinear controller is designed to modify the γ-parameters based on the state on the switching surface. The control design is motivated by insight into controlling simpler, hopper models, such as the SLIP. Based on the speed difference from the current step and the fixed point value, γ_{Tor} is updated to lean the torso forward to increase speed, or back to decrease speed. Further, as speed increases, the energy injected during the stance-decompression phase decreases because the time spent in this phase decreases with increasing speed. To account for this, the position of the stance-compression to stance-decompression transition is shifted, by updating $\gamma_{\delta_{sc\to sd}}$, to effectively increase or decrease the time spent injecting energy in the stance-decompression phase. Next, as discussed above, the knee angle at impact is important. As suggested by Rummel and Seyfarth in (Rummel and Seyfarth, 2008), for segmented legs with compliance in the joints, larger leg compression is required to produce the same leg force when the rest position of the spring is displaced from that corresponding to a straight leg. Since, for MABEL, the rest position of spring is essentially the impact angle of the knee (the spring is at its rest position during the flight phase), if the knee is bent an additional amount at impact, the leg must collapse even further to produce adequate restoring spring force to support the weight of the robot. To counteract this, $\gamma^{sc}_{k_{\mathrm{vc}}}$ adjusts the virtual compliance based on the impact angle of the knee. Further in anticipation of the additional bend in the stance knee, the swing leg knee is further bent through $\gamma_{\mathrm{LS}_{\mathrm{sw}}}$ to assure ground clearance.

The control law Γ^{γ} is summarized as

$$\begin{aligned}
\gamma^{sc}_{k_{\mathrm{vc}}} &= \begin{cases} K_{k^{sc}_{\mathrm{vc}}}(q^{s+}_{\mathrm{LS}_{\mathrm{st}}} - q^{s+*}_{\mathrm{LS}_{\mathrm{st}}}), & q^{s+}_{\mathrm{LS}_{\mathrm{st}}} - q^{s+*}_{\mathrm{LS}_{\mathrm{st}}} > 0 \\ 0, & otherwise \end{cases} \\
\gamma_{\mathrm{Tor}} &= \begin{cases} K^{+}_{\mathrm{Tor}}(\dot{p}^{h,s+}_{\mathrm{hip}} - \dot{p}^{h,s+*}_{\mathrm{hip}}), & (\dot{p}^{h,s+}_{\mathrm{hip}} - \dot{p}^{h,s+*}_{\mathrm{hip}}) > 0 \\ K^{-}_{\mathrm{Tor}}(\dot{p}^{h,s+}_{\mathrm{hip}} - \dot{p}^{h,s+*}_{\mathrm{hip}}), & otherwise \end{cases} \\
\gamma_{\mathrm{LS}_{\mathrm{sw}}} &= \begin{cases} K_{\mathrm{LS}_{\mathrm{sw}}}(q^{s+}_{\mathrm{LS}_{\mathrm{st}}} - q^{s+*}_{\mathrm{LS}_{\mathrm{st}}}), & q^{s+}_{\mathrm{LS}_{\mathrm{st}}} - q^{s+*}_{\mathrm{LS}_{\mathrm{st}}} > 0 \\ 0, & otherwise \end{cases} \\
\gamma_{\delta_{sc\to sd}} &= \begin{cases} K_{\delta_{sc\to sd}}(\dot{p}^{h,s+}_{\mathrm{hip}} - \dot{p}^{h,s+*}_{\mathrm{hip}}), & (\dot{p}^{h,s+}_{\mathrm{hip}} - \dot{p}^{h,s+*}_{\mathrm{hip}}) > 0 \\ 0, & otherwise \end{cases}
\end{aligned} \tag{87}$$

where $q^{s+}_{\mathrm{LS}_{\mathrm{st}}}, \dot{p}^{h,s+}_{\mathrm{hip}}$ are the stance leg shape angle and the horizontal speed of the hip respectively at impact with the ground. The symbols with an asterisk in the superscript indicate their nominal fixed point values. The gains $K_{k^{sc}_{\mathrm{vc}}}, K^{+}_{\mathrm{Tor}}, K^{-}_{\mathrm{Tor}}, K_{\mathrm{LS}_{\mathrm{sw}}}, K_{\delta_{sc\to sd}}$ are iteratively found through simulations. Furthermore, the γ-parameters are bounded such that, $-\gamma^{sat} \leq \gamma \leq \gamma^{sat}$.

With this second outer-loop discrete event-based controller Γ^{γ}, the robustness to perturbations is increased and as shown in Figure 16(b), is able to reject a perturbation of 5° in the impact leg shape angle (knee being bent an additional 10°). The stability of the entire closed-loop system can be studied once more by looking at the eigenvalues of a Poincaré map. To do this we need to numerically compute the Poincaré map $P_{\gamma} : \mathcal{S}_{\gamma} \times \mathcal{B} \times \mathcal{G} \to \mathcal{S}_{\gamma}$. However, it is difficult to compute variations of the state to lie on $\mathcal{S}_{\gamma}$, instead we move it to a place where it is easier to compute these variations. We consider $\tilde{\mathcal{S}}_{\gamma} = \{x_s \in TQ_s \mid \theta_s = \theta_{77\%}\}$ which represents a switching surface 77% into the stance phase. We can then study the eigenvalues of the Poincaré map $\tilde{P}_{\gamma} : \tilde{\mathcal{S}}_{\gamma} \times \mathcal{B} \times \mathcal{G} \to \tilde{\mathcal{S}}_{\gamma}$. While the Poincaré section is changed for ease of computation of the eigenvalues, the β, γ parameters still continue to be updated on their respective switching surfaces $\mathcal{S}_{\beta}$ and $\mathcal{S}_{\gamma}$. To define the Poincaré map $\tilde{\mathcal{P}}_{\gamma}$, we define three maps: $\tilde{P}^{1}_{\gamma} : \tilde{\mathcal{S}}_{\gamma} \times \mathcal{B} \times \mathcal{G} \to \mathcal{S}_{\gamma}$ which maps a state on $\tilde{\mathcal{S}}_{\gamma}$ along with β and γ parameters onto the post-impact surface, which is also the switching surface $\mathcal{S}_{\gamma}$ for the event-based controller Γ^{γ}; $\tilde{P}^{2}_{\gamma} : \mathcal{S}_{\gamma} \times \mathcal{B} \times \mathcal{G} \to \mathcal{S}_{\beta}$ which maps a state on $\mathcal{S}_{\gamma}$ onto the stance-compression to stance-decompression transition surface, which is also the switching surface $\mathcal{S}_{\beta}$ for the event-based controller Γ^{β}; and finally $\tilde{P}^{3}_{\gamma} : \mathcal{S}_{\beta} \times \mathcal{B} \times \mathcal{G} \to \tilde{\mathcal{S}}_{\gamma}$, which maps a state on $\mathcal{S}_{\beta}$ back onto $\tilde{\mathcal{S}}_{\gamma}$, the Poincaré section under consideration. To further clarify this, we define,

$$\begin{aligned} x^{a}_{p}[k] &= \tilde{\mathcal{P}}^{1}_{\gamma}(x_p[k], \beta[k], \gamma[k]) && (88) \\ x^{b}_{p}[k] &= \tilde{\mathcal{P}}^{2}_{\gamma}(x^{a}_{p}[k], \beta[k], \Gamma^{\gamma}(x^{a}_{p}[k])). && (89) \end{aligned}$$

Then,

$$\begin{aligned} x_p[k+1] &= \tilde{\mathcal{P}}_{\gamma}(x_p[k], \beta[k], \gamma[k]) \\ &= \tilde{\mathcal{P}}^{3}_{\gamma}\left(x^{b}_{p}[k], \Gamma^{\beta}(x^{b}_{p}[k]), \Gamma^{\gamma}(x^{a}_{p}[k])\right) \end{aligned} \tag{90}$$

Thus the γ parameters continue to be updated on the switching surface $\mathcal{S}_\gamma$, while the β parameters are updated on the switching sruface $\mathcal{S}_\beta$. The switching section $\tilde{\mathcal{S}}_\gamma$ serves only to define the Poincaré map $\tilde{\mathcal{P}}_\gamma$. With this, the eigenvalues of the linearized Poincaré map was computed and a dominant eigenvalue of 0.6072 was obtained indicating that the closed-loop system still remains exponentially stable.

***Remark** 1:* Note that the designs of the controllers $\Gamma^\alpha, \Gamma^{\alpha_c}, \Gamma^\beta$ are carried out through rigorous mathematical techniques, whereas the design of the outer-loop controller Γ^γ is based on heuristics. It is noted that the controllers $\Gamma^\alpha, \Gamma^{\alpha_c}, \Gamma^\beta$ achieve stable running in simulations on the design model. The controller Γ^γ aids in the experimental validation of running by increasing the closed-loop system's robustness to perturbations in the knee angle at impact and to imperfections in the ground contact model. Section VII provides additional comments in this regard. Nonetheless, as shown, the stability of the entire closed-loop system with the controllers $\Gamma^\alpha, \Gamma^{\alpha_c}, \Gamma^\beta$, and Γ^γ can still be studied by looking at the eigenvalues of a Poincaré map.

B. Two Models for Design and Verification : Simple vs Detailed Model

All control design in this paper is based on the model developed in Section II, henceforth called the *simple model*. This model made certain assumptions about the robot and its interaction with the ground: (a) rigid impacts; (b) the cables in the transmission of the robot do not stretch; and (c) the robot is planar. Controllers designed with the simple model worked well in walking experiments, as reported in (Sreenath et al., 2011). However, when the simple model was used to design a controller for hopping on two feet, sustained hopping was never achieved, as reported in (Park et al., 2011). This motivated the development of a *more detailed model* in (Park et al., 2011).

The detailed model includes: (a) a compliant ground model that includes slipping; (b) stretchy cables; and (c) boom dynamics.

We expect running to more closely resemble hopping than walking. Hence, a controller that works on the detailed model is sought. Performing control design with the detailed model is hard since the optimization required to find periodic running gaits is not computationally tractable. Instead, control design is carried out on the simple model and prior to experimental deployment, the designed running controller is verified on the detailed model. If the designed controller can not exhibit stable running motions on the detailed model, appropriate modifications need to be made to the controller. In the following section, modifications to account for cable stretch are presented. Potential modifications to account for asymmetry and compliant ground model are suggested in Section VI.

TABLE I
STIFFNESS CONSTANTS FOR VARIOUS SOURCES OF COMPLIANCE.

Source of compliance	**Stiffness value**
k_{Bsp}	3.17
k_{cable}	2.46
k^*_{vc}	1.66
k_{vc}	5.08

C. Modifications to account for Cable Stretch

For running, cable stretch in the leg shape joint reaches a peak of almost 15° (in the leg shape coordinates) just prior to lift-off. The nominal peak leg shape is around 25° (see Fig. 8.) Seen in another way, over 60% of motion in the knee is due to cable stretch. This results in excessive knee bending and causes the nominal controller to fail. A controller that can account for this severe cable stretch is then required.

The cable stretch in the leg shape joint can be modeled as a spring (with damping) and placed in series with the virtual compliant leg. This causes the compliance due to cable stretch to appear in series with the physical compliance and the motor leg shape actuator. Since the controller presented in the previous sections utilized active force control to create a virtual compliant element, all three sources of compliance, $k_{\mathrm{Bsp}}, k_{\mathrm{vc}}, k_{cable}$, occur in series. The optimization process produced a particular spring stiffness for the virtual compliance, k^*_{vc}. Using the active force control, the virtual compliance can be changed such that the compliance due to the cable stretch and the virtual compliance in series together has the effective compliance of that designed by the optimization process, i.e.,

$$\frac{1}{k_{cable}} + \frac{1}{k_{\mathrm{vc}}} = \frac{1}{k^*_{\mathrm{vc}}}. \tag{91}$$

With this modification, the effective compliance of the leg is now the same as that without cable stretch, i.e., cable stretch has been accounted for by the control design. Table I enumerates the stiffness values for the various compliances discussed here.

With these modifications, the running controller is ready for experimental deployment.

***Remark** 2:* One would expect the cables to have a large stiffness. However, from Table I, the cables appear to be softer than the physical spring by 20%, suggesting that the cable stretch contributes as much as the spring to the compliance present in the system.

V. RUNNING EXPERIMENTS

This section documents experimental implementations of the running controller developed in Sections III, IV in various running scenarios. To illustrate the power and limitations of the proposed method, three experiments are presented. The first experiment details the execution of a transition controller that transitions from walking to running, the second experiment details a running experiment, and finally the third experiment details the transition from running to walking. Point feet are used for all experiments in this section.

As in the walking experiments reported in (Sreenath et al., 2011), the controller was first coded in C++ and evaluated on a detailed simulation model of the robot that included encoder quantization and numerical estimation of velocity variables from encoder measurements. The controller was tested under various model perturbations, such as errors in the torso mass, spring stiffness, torso center of mass position, and deviations in initial conditions. The simulation model was then replaced with the physical robot.

In the experiments, the left leg refers to the inner leg, which is closer to the center boom, and the right leg refers to the outer leg, which is farther from the center boom. All running speeds are measured with respect to the center point of the hip between the two legs. Videos of the experiments are available on YouTube (Grizzle, 2010a).

A. *Exp. 1: Two-step Transition from Walking to Running*

Experimentally, MABEL cannot be initialized in running; the robot must first walk and then transition into running. The transition must ensure that the initial conditions are sufficiently close to the periodic orbit for running. The running controller is executed on completion of the transition.

To transition from walking to running, a transition controller based on (Westervelt et al., 2003) is developed which modifies the virtual constraints of the fixed point for walking to bring the virtual constraint at the end of the walking gait closer to the corresponding virtual constraint at the beginning of the running gait. Instead of a one-step transition from walking to running as done in (Morris et al., 2006), for MABEL, a two-step transition is carried out. Essentially, there are two transition steps, with the first step being a transition-walk-step, and the second step being a transition-run-step. A walk-to-run transition then consists of the following: (a) A transition from the nominal walking gait to the transition-walk-step, followed by (b) a transition from the transition-walk-step to the transition-run-step, and finally (c) a transition from the transition-run-step to the nominal running gait. This two-step transition enables a smoother transition and prevents rapid torso motions, especially on gaits where the ending and beginning values of the torso virtual constraint differ significantly for the walking and running fixed points respectively. Figure 17(a,c,e,g) illustrate plots of various variables for the transition from walking to running. The walking and running sections are clearly marked along with the two transition steps.

B. *Exp. 2: Running with Point Feet*

Initial experiments on MABEL failed to achieve steady-state running due to the foot slipping and an inability to regulate speed. We attribute these failures to imperfections in the ground contact model used in the controller design. To address these issues, the point-feet were replaced with passive feet with shoes, the idea being that the feet and shoes would provide a larger surface area for traction, thereby preventing slipping, and the softer impacts with the shoes would potentially slow down the robot. Successful running was achieved. Appendix A provides more details on these experiments.

The lessons learned from steady-state running with passive feet are used to implement the running controller when the robot is equipped with point feet. Firstly, to address slipping, an anti-slip track is installed in the lab (see Figure 18(a)). Next, the method of speed regulation that was effective for running with passive feet is employed for running with point feet.

Thus, for running with point feet, the following modifications to the running controller presented in Sections III, IV are performed. As suggested in Appendix A, for speed regulation, the γ-parameter corresponding to the virtual compliance stiffness is modified as in (94). The saturation for β-parameter corresponding to the touch down angle is modified as in (95). The saturation for the γ-parameter that modifies the location of the stance-compression to stance-decompression phase is also modified as a function of the speed and is given as,

$$\gamma^{sat}_{\delta_{sc\to sd}} = \begin{cases} 0.2, & 0 \le \dot{p}^{h,avg}_{\text{hip}} < 2 \\ 0.25, & 2 \le \dot{p}^{h,avg}_{\text{hip}} < 2.5 \; . \\ 0.35, & 2.5 \le \dot{p}^{h,avg}_{\text{hip}} \end{cases} \tag{92}$$

At high speeds, the time spent in the stance-decompression phase decreases, which results in less energy being injected and smaller push-offs. With the above modification, a well defined flight phase is maintained even when running fast.

Next, to prevent the stance-decompression phase from causing a lift-off with a high velocity, the stance-decompression to flight phase switching surface is modified as follows

$$\mathcal{S}^{exp}_{sd\to \text{f}} := \mathcal{S}_{sd\to \text{f}} \cap \{x_{\text{s}} \in TQ_{\text{s}} \mid \dot{p}^{v}_{\text{hip}} > \dot{p}^{v,s-*}_{\text{hip}}\}. \tag{93}$$

In addition, during the stance-decompression phase, the torso is pushed back in a similar manner as in the running with feet experiment. Finally, during the flight phase, the adaptive correction polynomials, as used for the running with feet experiment, are deployed. Both these changes counteract the effect of unmodeled cable stretch in the leg angle direction.

With these changes to the controller developed in Sections III, IV, the running experiment is carried out as follows. First, walking is initiated on MABEL using the walking controller developed in (Sreenath et al., 2011). Next, the walking to running transition controller, presented in Section V-A, is executed. Finally, on transition to running, the running controller is executed. The running controller induced stable running at an average speed of 1.95 m/s, and a peak speed of 3.06 m/s. 113 running steps were obtained and the experiment terminated when the power to the robot was cut off. At 2 m/s, the average stance and flight times of 233 ms and 126 ms are obtained respectively, corresponding to

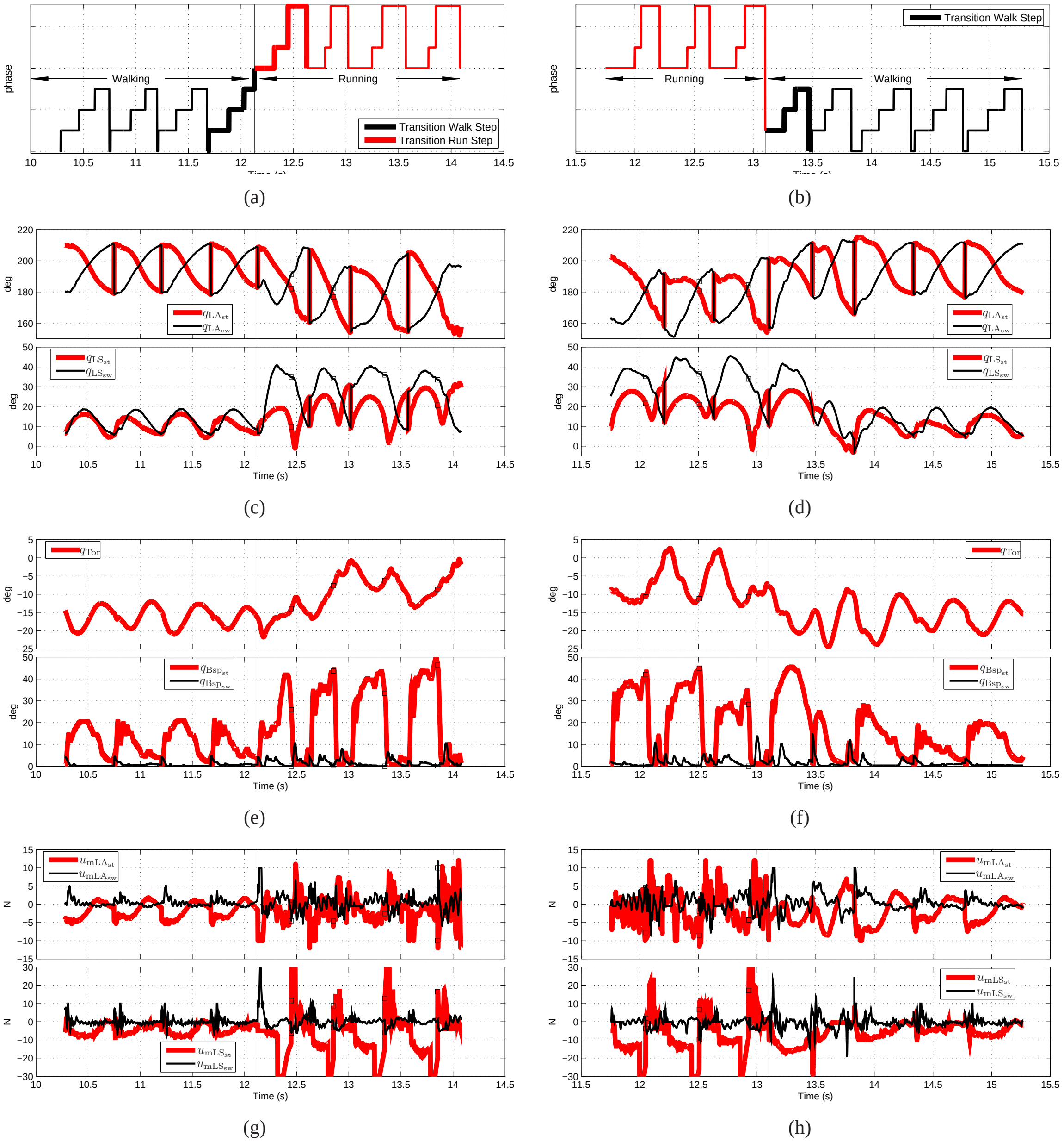

(a) (b)

(c) (d)

(e) (f)

(g) (h)

Fig. 17. Experimental plots for (a,c,e,g) transition from walking to running (Exp. 1) and (b,d,f,g) transition from running to walking (Exp. 3). (a,b) depict internal phase variable of the controller and indicate the walking and running parts of the gait. The thicker plots indicate the transition steps. For transition to running there are two transition steps - one during walking and the other during running, while for transition to walking there is one transition step during walking. (c,d) illustrate the leg angle and leg shape variables for the stance and swing legs. (e,f) illustrate the torso and stance and swing bspring variables. The peak spring compression for running is around 2.5 times that for walking. (g,h) illustrate the torques for the leg angle and leg shape motors for the stance and swing legs.

a flight phase that is 35% of the gait. At 3 m/s, the average stance and flight times of 195 ms and 123 ms are obtained respectively, corresponding to a flight phase that is 39% of the gait. An estimated ground clearance of $3-4$ inches ($7.5-10$ cm) is obtained. The specific cost of mechanical transport (c_{mt}), defined in (Collins and Ruina, 2005), was computed to be 1.07.

Figure 18(a) depicts snapshots at 100 ms intervals of a typical running step. Figure 19(a) depicts the mean joint angles, temporally normalized over time, for 50 consecutive steps of running.

The outer-loop event based controller parameters are depicted in Figures 21(a), 22(a). There is considerable variation in speed. When the speed exceeds 2.5 m/s, large changes in the touch down angle, β_{TD}, and the γ-parameter that affects the transition from stance-compression to stance-decompression, $\gamma_{\delta_{sc\rightarrow sd}}$ causes the speed to dramatically drop to under 1 m/s. All this is autonomously handled by the controller with no manual intervention. The ability of the controller to recover from slow speeds below 1 m/s, and high speeds above 2.5 m/s illustrates a good robustness to imperfections in the ground contact model. The controller is also able to account for significant cable stretch (shown in Figure

(a) (b)

Fig. 18. Snapshots of a typical running step for (a) running with point-feet, and (b) running with passive feet, are shown at intervals of 100 ms. The snapshots progress temporally from left to right and from top to bottom.

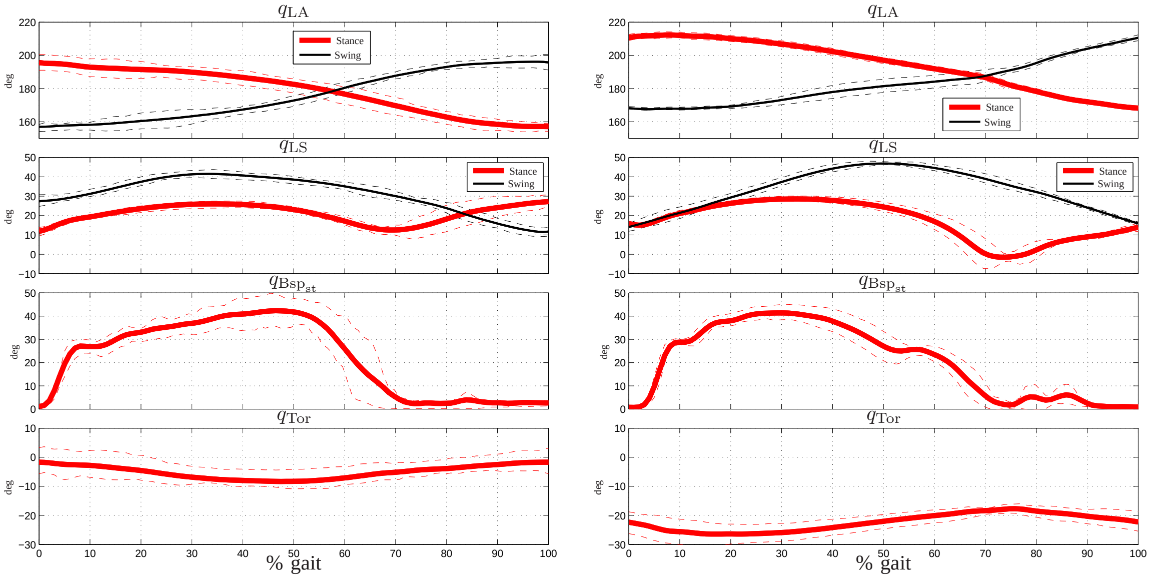

(a) (b)

Fig. 19. Ensemble plots of joint angles of the stance and swing legs for 50 consecutive steps of (a) running with point-feet, and (b) running with passive feet. The solid lines represent the mean recorded joint angle waveforms, while the dotted lines indicate the upper and lower quartiles over the running steps. The curves were temporally normalized from initial touchdown (0%) to subsequent touchdown (100%).

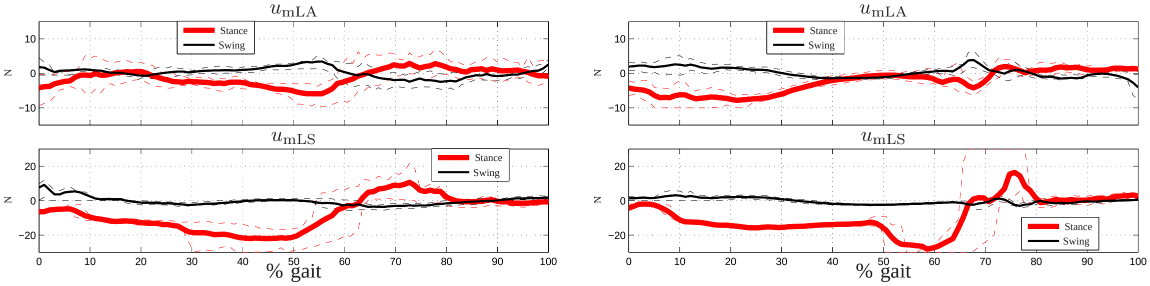

(a) (b)

Fig. 20. Ensemble plots of motor torques for the stance and swing legs for 50 consecutive steps of (a) running with point-feet, and (b) running with passive feet. The solid lines represent the mean recorded torque waveforms, while the dotted lines indicate the upper and lower quartiles over the running steps. The curves were temporally normalized from initial touchdown (0%) to subsequent touchdown (100%).

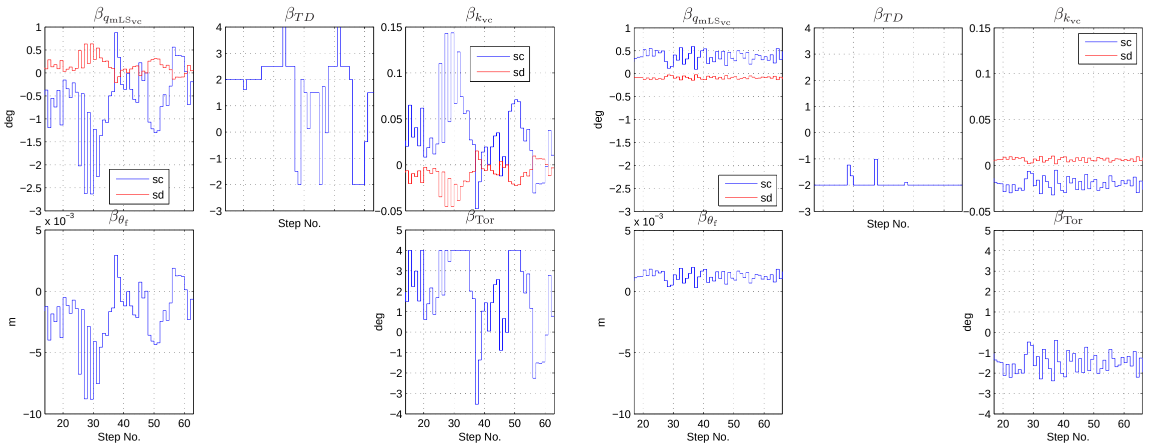

(a) (b)

Fig. 21. Parameter plots for 50 consecutive steps for the outer-loop event-based controller, Γ^{β}, for (a) running with point-feet and (b) running with passive feet. sc, sd refer to the values of the corresponding β-parameters in the stance-compression and stance-decompression subphases respectively.

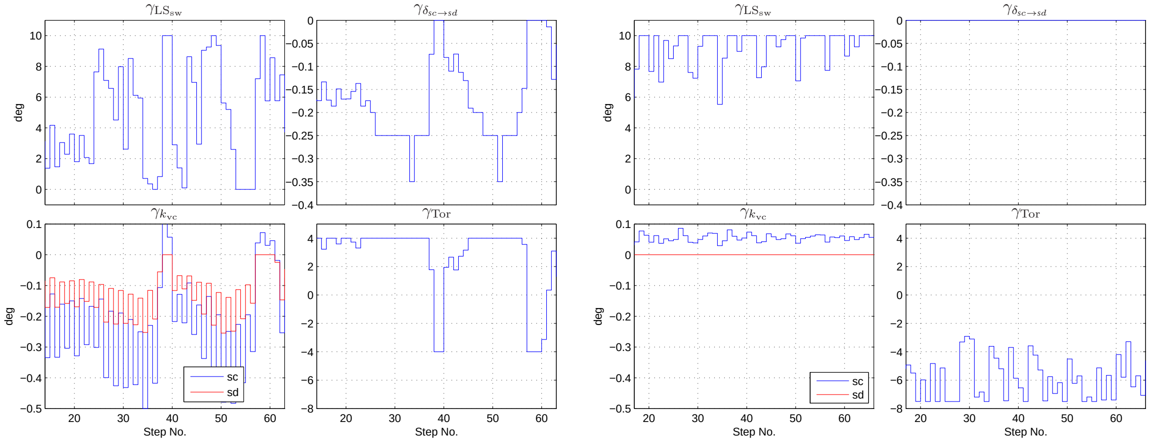

(a) (b)

Fig. 22. Parameter plots for 50 consecutive steps for the nonlinear outer-loop controller for increasing robustness to perturbations , Γ^{γ}, for (a) running with point-feet and (b) running with passive feet. sc, sd refer to the values of the corresponding γ-parameters in the stance-compression and stance-decompression subphases respectively.

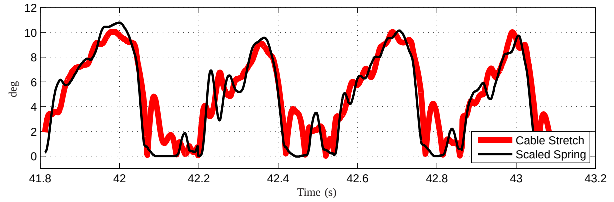

Fig. 23. Absolute value of leg shape cable stretch and spring compression for the stance leg for the running with point-feet (Exp. 2.). Both variables are scaled to be in the leg shape coordinates. As is seen, cable stretch contributes as much as the spring to the compliance present in the system. This was hinted at in Table I.

23.)

C. Exp. 3: One-step Transition from Running to Walking

This section details a transition controller that transitions from running to walking. The method of active force control (introduced in Section III-E) within the compliant hybrid zero dynamics to create a virtual compliant element is capable of accommodating large impacts with the ground while mainting good ground reaction forces. This has been observed in the running experiments and also for large step-down experiments (see (Park et al., 2012).) To obtain a transition from running to walking, the running controller is switched to the walking controller with virtual compliance that was used successfully for the step-down experiments. The transition from running to walking is then considered as a large step-down by the walking controller. After the single transition step, the nominal walking controller is executed and transition to walking is obtained.

Figure 17(b,d,f,h) illustrate plots of various variables for the transition from running to walking. The running and walking sections are clearly marked along with the transition step.

VI. DISCUSSION OF THE EXPERIMENTS

This section discuss various aspects of the robot and the feedback controller that are revealed by the experiments.

A. Impact Model

The ground contact is the weakest part of our model. As observed in walking experiments on MABEL (Sreenath et al., 2011), for running, the robot ran faster than predicted by both dynamic models: (a) rigid impacts (simple model) and (b) the compliant ground model (detailed model.) For legged robots, the accuracy of the model of the impact with the ground surface is difficult to ascertain and to improve. (Sreenath et al., 2011, Sec. VII-B) cites various ways of modeling the ground impact and presents impact scaling to account for speed differences in walking for MABEL. For the running controller demonstrated here, the ground contact model needs the most improvement. It is unknown if the parameters in the present compliant ground model can be tuned to account for the experimental results.

B. Asymmetry

The model used in the feedback designs has assumed a planar root. Whereas, in the experimental setup, due to the boom, the robot's hip position is constrained to lie on the surface of a sphere, rather than a plane. As discussed in Section IV-B, the detailed model captures asymmetry as part of the model by incorporating boom kinematics and dynamics. This also accounts for the hip width (distance between the legs) being 10% of the length of the boom, which causes the robot to weigh 10% more when supported on the inner leg (almost 7 Kg) than when supported on the outer leg. For running, this causes problems. The impacts on the inside leg are harder and cause the stance knee to bend more, and this in turn causes the outer-loop controller to overcompensate in the following step (notice the prounced step-to-step oscillations in the virtual compliance stiffnes in Figure 22(a).)

To potentially account for this, the following changes are suggested. Since the controller in the stance phase creates a virtual compliant element, the virtual compliance could be made an additional 10% stiffer on the inside leg. Moreover, for smoother running motions, the outer-loop controllers have to perform separate step-to-step updates over two steps.

C. Moving Heuristics to Analysis

The running controller developed has multiple loops, Γ^{α}, Γ^{α_c}, Γ^{β}, and Γ^{γ}. The inner-loops, Γ^{α}, Γ^{α_c}, and Γ^{β}, are auto designed using rigorous analytical techniques. Γ^{α}, and Γ^{β} are partly driven by the morphology of the bipedal robot since the choice of the virtual constraints and the β-parameters is partly dependent on the morphology. The outer-loop event-based controller, Γ^{γ}, is however essentially based on heuristics. The question that remains unanswered is, can this outer-loop controller be analytically designed?

Firstly, even in the absence of Γ^{γ}, the designed controller creates an exponentially stable periodic orbit. The outer-loop event-based controller Γ^{γ} is added to increase the robustness (to perturbations in the knee angle at impact and to imperfections in the ground contact model) of the designed running controller for experimental deployment. If the design model matched closely with the physical system, speed regulation would not be an issue, as it would have been taken care by the exponentially stabilizing event-based controller Γ^{β}. Nevertheless, analytically estimating the domain of attraction for a periodic solution for a complex system such as MABEL, and then designing controllers to increase this domain, thereby improving robustness to perturbations, is an extremely hard problem.

One way to analytically design the final layer of the controller would be to come up with the reduced order system, or some mechanical analog, representing the zero dynamics. Once such a system is available, then analytical methods can be used to design a controller for this system. However, coming up with the reduced order system is non-trivial. One way to analytically design a controller to perform speed regulation would be to carry out energy regulation (Poulakakis and Grizzle, 2009b). However, this requires estimating the kinetic and potential energies, typically very noisy quantities in real experiments. Thus, the problem of analytically designing a practical Γ^{γ} controller for increasing robustness to perturbations is still an open problem and needs to be investigated further.

Alternatively, numerical techniques such as approximate dynamic programming can be utilized to compute optimal outputs of the Γ^{γ} controller for a particular perturbation. However, this approach would be computationally expensive depending on the number of the states and their respective discretizations.

VII. CONCLUSION

MABEL contains springs in its drivetrain for the purposes of enhancing agility and robustness of dynamic locomotion. This paper has presented a model-based control design method to realize the potential of the springs. Experiments have been performed to illustrate and confirm important aspects of the feedback design.

The controller is based on the hybrid zero dynamics introduced in (Poulakakis and Grizzle, 2009b) and further developed and deployed experimentally in (Sreenath et al., 2011). An important modification was the deliberate inclusion of actuation in the zero dynamics during the stance phase of running, which enabled active force control of the stance knee. Specifically, a virtual compliant element was created to dynamically vary the effective leg compliance during stance. An outer-loop event-based controller was designed to exponentially stabilize the periodic running gait. An additional outer-loop event-based controller was designed to improve the robustness of the periodic running gait to perturbations in the knee angle at impact and to imperfections in the ground contact model.

The running controller has been experimentally deployed and stable running has been successfully demonstrated on MABEL, both with passive feet and with point feet. The achieved running is dynamic and life-like, exhibiting flight phases of significant duration and high ground clearance. For running with point feet, a peak speed of 3.06 m/s (6.8 mph) was obtained, making MABEL the fastest kneed bipedal runner as of July 30, 2011.

Acknowledgments

The authors are grateful to A. Ramezani for his expert help with the experiments. K. Sreenath acknowledges L. McCauley for suggesting the experiments with nontrivial feet, and B. Morris is thanked for his advice - “Go big, or go home,” which helped us to focus on multiple steps of running, and for his contributions to the theoretical underpinnings of our work, as cited in the text. I.Poulakakis is acknowledged for providing inspiration and for introducing compliance into the framework of hybrid zero dynamics. J. Konscol is thanked for his weekly visits to the lab and for sharing his engineering experience, which contributed invaluably to the robustness of the electronic setup of the testbed. G. Buche is thanked for his many contributions to the design of the electronics, power supply, and safety interlock systems. Last but not least, we are deeply indebted to J. Hurst for designing MABEL. We hope that this paper has once again confirmed many of his expectations for the robot.

REFERENCES

Cavagna, G. A., Thys, H., and Zamboni, A. (1976). The sources of external work in level walking and running. *Journal of Physiology*, 262:639–657.

Chevallereau, C., Grizzle, J. W., and Shih, C.-L. (2009). Asymptotically stable walking of a five-link underactuated 3d bipedal robot. *IEEE Transactions on Robotics*, 25(1):37–50.

Cho, B.-K., Park, S.-S., and ho Oh, J. (2009). Controllers for running in the humanoid robot, HUBO. In *IEEE-RAS International Conference on Humanoid Robots*, pages 385–390, Paris, France.

Choi, J. H. and Grizzle, J. W. (2005). Planar bipedal walking with foot rotation. In *American Control Conference*, pages 4909–4916, Portland, Oregon.

Collins, S. H. and Ruina, A. (2005). A bipedal walking robot with efficient and human-like gait. In *IEEE International Conference on Robotics and Automation*, pages 1983–1988, Barcelona, Spain.

Daley, M. A. and Biewener, A. A. (2006). Running over rough terrain reveals limb control for intrinsic stability. *Proceedings of the National Academy of Sciences of the United States of America*, 103(42):15681–15686.

Daley, M. A., Usherwood, J. R., Felix, G., and Biewener, A. A. (2006). Running over rough terrain: guinea fowl maintain dynamic stability despite a large unexpected change in substrate height. *The Journal of Experimental Biology*, 209:171–187.

Ferris, D. P. and Farley, C. T. (1997). Interaction of leg stiffness and surface stiffness during human hopping. *Journal of applied physiology*, 82:15–22.

Ferris, D. P., Louie, M., and Farley, C. T. (1998). Running in the real world: adjusting stiffness for different surfaces. *Proceedings of The Royal Society*, 265(1400):989–994.

Full, R. J. and Koditschek, D. E. (1999). Templates and anchors: Neuromechanical hypotheses of legged locomotion on land. *The Journal of Experimental Biology*, 202(23):3325–3332.

Grizzle, J. W. (2010a). Dynamic leg locomotion. Youtube Channel: http://www.youtube.com/DynamicLegLocomotion.

Grizzle, J. W. (2010b). Jessy Grizzle’s publications. http://www.eecs.umich.edu/~grizzle/papers/robotics.html.

Grizzle, J. W., Chevallereau, C., and Shih, C.-L. (2008). HZD-based control of a five-link underactuated 3d bipedal robot. In *IEEE Conference on Decision and Control*, Cancun, Mexico.

Grizzle, J. W., Hurst, J., Morris, B., Park, H.-W., and Sreenath, K. (2009). MABEL, a new robotic bipedal walker and runner. In *American Control Conference*, pages 2030–2036, Saint Louis, MO, USA.

Hirose, M. and Ogawa, K. (2007). Honda humanoid robots development. *Philosophical Transactions of The Royal Society A*, 365(1850):11–19.

Hurmuzlu, Y. and Marghitu, D. B. (1994). Rigid body collisions of planar kinematic chains with multiple contact points. *The International Journal of Robotics Research*, 13(1):82–92.

Hurst, J. W. (2008). *The Role and Implementation of Compliance in Legged Locomotion*. PhD thesis, Carnegie Mellon University.

Isidori, A. (1995). *Nonlinear Control Systems*. Springer-Verlag, Berlin, third edition.

Kajita, S., Kaneko, K., and Morisawa, M. (2007). Zmp-based biped running enhanced by toe springs. In *IEEE International Conference on Robotics and Automation*, pages 3963–3969, Roma, Italy.

Kajita, S., Nagasaki, T., Kaneko, K., Yokoi, K., and Tanie, K. (2005). A running controller of humanoid biped hrp-2lr. In *IEEE International Conference on Robotics and Automation*, pages 616–622, Barcelona, Spain.

Koechling, J. C. (1989). *The limits of running speed: Experiments with a legged robot*. PhD thesis, Carnegie Mellon University, Pittsburgh, PA.

Koepl, D., Kemper, K., and Hurst, J. (2010). Force control for spring-mass walking and running. In *IEEE/ASME International Conference on Advanced*

Intelligent Mechatronics, pages 639–644, Montreal, Canada.

McGeer, T. (1990). Passive bipedal running. *Proceedings of the Royal Society of London*, 240(1297):107–34.

McMahon, T. A. and Cheng, G. C. (1990). The mechanics of running: How does stiffness couple with speed? *Journal of Biomechanics*, 23(1):65–78.

Morris, B. and Grizzle, J. W. (2005). A restricted Poincaré map for determining exponentially stable periodic orbits in systems with impulse effects: Application to bipedal robots. In *IEEE Conference on Decision and Control*, pages 4199–206, Seville, Spain.

Morris, B. J. and Grizzle, J. W. (2009). Hybrid invariant manifolds in systems with impulse effects with application to periodic locomotion in bipedal robots. *IEEE Transactions on Automatic Control*, 54(8):1751 – 1764.

Morris, B. J., Westervelt, E. R., Chevallereau, C., Buche, G., and Grizzle, J. W. (2006). *Achieving Bipedal Running with RABBIT: Six Steps Toward Infinity*, volume 340 of *Lecture Notes in Control and Information Sciences*, pages 277–297. Springer Berlin / Heidelberg.

Nagasaka, K., Kuroki, Y., Itoh, S., and Yamaguchci, J. (2004). Integrated motion control for walking, jumping and running on a small bipedal entertainment robot. In *IEEE International Conference on Robotics and Automation*, pages 3189–3194, New Orleans, LA.

Park, H.-W., Sreenath, K., Hurst, J. W., and Grizzle, J. W. (2011). Identification of a bipedal robot with a compliant drivetrain: Parameter estimation for control design. *Control Systems Magazine*, 31(2):63–88.

Park, H.-W., Sreenath, K., Ramezani, A., and Grizzle, J. W. (submitted, 2012). Switching control design for accommodating large step-down disturbances in bipedal robot walking. In *IEEE International Conference on Robotics and Automation*.

Poulakakis, I. and Grizzle, J. W. (2009a). Modeling and control of the monopedal robot thumper. In *IEEE International Conference on Robotics and Automation*, pages 3327–3334, Kobe, Japan.

Poulakakis, I. and Grizzle, J. W. (2009b). The spring loaded inverted pendulum as the hybrid zero dynamics of an asymmetric hopper. *IEEE Transactions on Automatic Control*, 54(8):1779–1793.

Rummel, J. and Seyfarth, A. (2008). Stable running with segmented legs. *The International Journal of Robotics Research*, 27(8):919–934.

Sreenath, K., Park, H.-W., Poulakakis, I., and Grizzle, J. W. (2011). Compliant hybrid zero dynamics controller for achieving stable, efficient and fast bipedal walking on MABEL. *International Journal of Robotics Research*, 30(9):1170–1193.

Tajima, R., Honda, D., and Suga, K. (2009). Fast running experiments involving a humanoid robot. In *IEEE International Conference on Robotics and Automation*, pages 1571–1576, Kobe, Japan.

Westervelt, E. R. (2003). *Toward a Coherent Framework for the Control of Planar Biped Locomotion*. PhD thesis, University of Michigan.

Westervelt, E. R., Grizzle, J. W., Chevallereau, C., Choi, J. H., and Morris, B. (2007). *Feedback Control of Dynamic Bipedal Robot Locomotion*. Taylor & Francis/CRC Press, Boca Raton, FL.

Westervelt, E. R., Grizzle, J. W., and de Wit, C. C. (2003). Switching and PI control of walking motions of planar biped walkers. *IEEE Transactions on Automatic Control*, 48(2):308–312.

APPENDIX A
RUNNING WITH PASSIVE FEET

Early running experiments always terminated either due to foot slipping, an inability to regulate speed, or other hardware issues. To address the issue of slipping and potentially that of speed regulation, the following hardware modifications were made on MABEL. The shins terminating with point feet were replaced with shins terminating in passive feet, enclosed within regular running shoes. The idea being that the feet would provide a larger surface area for better traction, thereby avoiding slipping and that the softer impacts would potentially slow down the robot.

With the addition of the passive feet, the dynamical model for running developed in Section II is no longer valid due to the following reasons: (a) the shins with feet are twice as heavy as the ones before, (b) the inertia properties significantly differ, and moreover, (c) the impacts are softer, with the shoes causing a rolling surface contact with the ground (instead of a point contact). Although it will be a good exercise to model the modified system with feet, however we carry out a few exploratory experiments instead to make modifications to the developed controller to obtain stable running on the modified system.

Modifications to regulate speed: Although the softer impacts with the ground due to the feet were expected to slow down the robot, speed regulation was not achieved. At faster speeds, the time spent in the stance-decompression phase decreased, thereby reducing the effective energy injection resulting in a lower peak apex height in flight. However, for running, an increase in kinetic energy cannot be rejected by a corresponding decrease in potential energy (Cavagna et al., 1976). Hence, to maintain a well defined flight phase at fast speeds, an additional parameter, $\gamma_{\delta_{sc\to sd}}$ (see (87)), was added to the outer-loop Γ^γ to modify the location of the stance-compression to stance-decompression switching surface.

Next, as suggested in (McGeer, 1990; McMahon and Cheng, 1990), animals vary stance leg stiffness to regulate running speed. Thus, there is a need for the controller to change the effective leg compliance as a function of speed. This is achieved by adding an additional term $\Delta\gamma^{sc}_{k_{\mathrm{vc}}}$ to $\gamma^{sc}_{k_{\mathrm{vc}}}$ computed in (87), where,

$$\Delta\gamma^{sc}_{k_{\mathrm{vc}}} := \begin{cases} -K_{k^{\mathrm{sc}}_{\mathrm{vc}}}\sqrt{\Delta\dot{p}^{h,avg}_{\mathrm{hip}}}, & \Delta\dot{p}^{h,avg}_{\mathrm{hip}} > 0 \\ 0, & otherwise \end{cases}, \tag{94}$$

with, $\Delta\dot{p}^{h,avg}_{\mathrm{hip}} = (\dot{p}^{h,avg}_{\mathrm{hip}} - \dot{p}^{h,avg*}_{\mathrm{hip}})$, and $\dot{p}^{h,avg*}_{\mathrm{hip}}$, $\dot{p}^{h,avg}_{\mathrm{hip}}$ being the nominal and last step average horizontal hip speeds respectively.

Finally, to enable large touchdown angles at faster speeds to effectively slow down the robot and to prevent large touchdown angles at slow speeds from causing the foot to slip, the β-parameters are bounded, such that, $-\beta^{sat} \leq \beta \leq \beta^{sat}$, with the saturation for the β-parameter corresponding to touchdown, β_{TD}, specified as a function of speed, as below,

$$\beta^{sat}_{TD} = \begin{cases} 2^\circ, & 0 \leq \dot{p}^{h,avg}_{\mathrm{hip}} < 1.2 \\ 1.5^\circ, & 1.2 \leq \dot{p}^{h,avg}_{\mathrm{hip}} < 1.7 \\ 2^\circ, & 1.7 \leq \dot{p}^{h,avg}_{\mathrm{hip}} < 2 \\ 2.5^\circ, & 2 \leq \dot{p}^{h,avg}_{\mathrm{hip}} < 2.5 \\ 4^\circ, & 2.5 \leq \dot{p}^{h,avg}_{\mathrm{hip}} \end{cases} \tag{95}$$

Modifications to account for the passive feet: The softer impacts due to the feet in the shoes result in the spring not compressing sufficiently and cause flight phases with smaller durations and with lower ground clearance. To account for the softer impacts, the nominal virtual compliance, k^*_{vc}, was reduced by 18%.

Next, during stance-decompression, energy injection causes the spring to first compress and then rapidly decompress resulting in rapid knee extension creating a push off. However, due to the geometry of the passive foot, specifically the absence of an ankle rotation DOF, when the leg is backward at the start of stance-decompression, only the forward part of the shoe is in contact with the ground. This causes a significant fraction of energy injection to be not translated into a push off, but rather rapidly affecting the angle of the foot with respect to the ground. This effect is more pronounced when the spring is close to its rest position. To address this, the stance-compression to stance-decompression switching surface is modified to ensure the switching occurs when the spring is sufficiently compressed,

$$\mathcal{S}^{exp}_{sc\to sd} := \mathcal{S}_{sc\to sd} \cap \{x_{\mathrm{s}} \in TQ_{\mathrm{s}} \mid \theta_{\mathrm{s}} > \theta_{50\%},\ q_{\mathrm{Bsp_{st}}} < 20^\circ\}, \tag{96}$$

where, $\theta_{50\%}$ represents the value of θ_{s} at 50% into the stance phase.

Next, to prevent (a) the foot from slipping towards the end of stance when the stance forces are small, (b) hyper-extension of the heavy shin, and (c) large vertical velocities at liftoff, the stance-decompression to flight switching surface is modified as below,

$$\begin{aligned} \mathcal{S}^{exp}_{sd\to\mathrm{f}} := \mathcal{S}_{sd\to\mathrm{f}} \cap \{x_{\mathrm{s}} \in TQ_{\mathrm{s}} \mid q_{\mathrm{Bsp_{st}}} < 15^\circ, \\ q_{\mathrm{LS_{st}}} < 2^\circ\} \cap \{x_{\mathrm{s}} \in TQ_{\mathrm{s}} \mid \dot{p}^{v}_{\mathrm{hip}} > \dot{p}^{v,s-*}_{\mathrm{hip}}\}, \end{aligned} \tag{97}$$

where, $\dot{p}^{v}_{\mathrm{hip}}$ is the vertical hip velocity, and $\dot{p}^{v,s-*}_{\mathrm{hip}}$ is the nominal liftoff vertical hip velocity.

Finally, to prevent the toes of the shoes from scuffing the ground during leg swing, the swing leg shape virtual constraint is modified such that it is commanded to fold by an additional constant amount.

Modifications to account for unmodeled cable stretch in leg angle transmission: The running controller accounts for unmodeled cable stretch in the leg shape coordinates, but not the leg angle coordinates. During the stance-decompression phase, the nominal virtual constraint for the torso specifies the torso to pitch backward. In experiments, the torso is sometimes driven forward to correct tracking errors, which results in the torso having a forward velocity at liftoff and causes the torso to pitch forward further during flight resulting in a significant torso error on impact. Large torques to correct this would then stretch the leg angle cables significantly. To prevent this, when the torso velocity drops below a threshold, the controller for the torso is switched to push the torso backward instead of trying to enforce a virtual constraint.

On initiation of the flight phase, the event-based controller $\Gamma^{\alpha_c}_{\mathrm{f}}$ ensures hybrid invariance of the flight zero dynamics manifold. This is done through correction polynomials, h^{f}_c as in (75), such that the modified virtual constraints smoothly join the nominal virtual constraints half-way into the flight phase. During experiments, large errors on initiation of the flight phase could result in the modified virtual constraint to initially reversing direction of motion, causing the leg angle cables to stretch significantly and resulting in large touchdown errors. To handle this, the correction polynomials are modified such that the modified virtual constraint smoothly joins the nominal virtual constraint at an adaptively chosen location that is either 50%, 75%, or 95% into the flight phase, depending on the sign and magnitude of the error on transition to the flight phase. These are termed *adaptive correction polynomials*.

With these changes to the controller, the running experiment with passive feet is carried out as follows. The walking controller developed in (Sreenath et al., 2011) is employed, along with a torso offset to lean the torso forward to induce stable walking with the passive feet at 1.26 m/s. The walking to running transition controller developed in section V-A is used to transition to running. On transition, the modified running controller described above is executed, resulting in stable running at an average speed of 1.07 m/s. 100 running steps were obtained and the experiment was terminated. Figure 18(b) illustrates snapshots of a typical step of running. Average stance and flight times of 360 ms and 151 ms are obtained respectively, corresponding to a flight phase that is 30% of the gait. An estimated ground clearance of around 2 inches (5 cm) is obtained. The specific cost of mechanical transport (c_{mt}) was computed to be 0.75.

Figure 19(b) depicts the mean joint angles, temporally normalized over time, for 50 consecutive steps of running. Figure 20(b) depicts the motor torques. Figures 21(b), 22(b) illustrates the β and γ-parameters for the 50 consecutive steps of running.